Highlights

Improving the Computation of Forced Responses of Periodic Structures by the Wave-based Finite Element Method via a Modified Generalized Bloch Mode Synthesis

Vinícius M. de S. Santos, Thiago de P. Sales, Morvan Ouisse

- The Generalized Bloch-Mode Synthesis (GBMS) and Wave-based Finite Element Method are combined
- Unit cell modal models of very small dimensions are derived
- Fast computation of accurate forced responses is achieved
- Minimal error metrics are demonstrated for the computed responses
- Mitigation of numerical issues is reported when combining the WFEM with the GBMS
- Best practices for analyzing structures using the WFEM and GBMS are provided

Improving the Computation of Forced Responses of Periodic Structures by the Wave-based Finite Element Method via a Modified Generalized Bloch Mode Synthesis

Vinícius M. de S. Santos[a,b], Thiago de P. Sales[a,*], Morvan Ouisse[b]

[a]*Mechanical Engineering Division, Aeronautics Institute of Technology, Praça Marechal Eduardo Gomes, 50, Vila das Acácias, São José dos Campos, 12228-900, SP, Brazil*
[b]*SUPMICROTECH, Université de Franche-Comté, CNRS, Institut FEMTO-ST, F-25000, Besançon, France*

Abstract

Periodic structures have attracted interest across various fields of science and engineering due to their unique ability to manipulate wave propagation. The Wave-based Finite Element Method (WFEM) is typically employed to model such systems by relying on the dynamic behavior of a single unit cell of the lattice. However, the WFEM can face challenges in handling unit cell finite element (FE) models with several degrees of freedom (DoFs), as it involves operating with large-sized matrices. Therefore, in this work, we combine the WFEM with the Generalized Bloch-Mode Synthesis (GBMS) to offer a highly efficient and accurate method for modeling periodic structures. Three different types of unit cells were investigated in this study, demonstrating that highly reduced unit cell models can be obtained using the Craig-Bampton (CB) and Local-level Characteristic Constraint (L-CC) model reduction methods. By leveraging the advantages of the WFEM and the reduced-order unit cell models, harmonic forced responses were rapidly and accurately computed. Additionally, we showed that combining the WFEM with the GBMS mitigates numerical issues when computing forced responses, as the boundary DoFs are reduced to a smaller number of equations, avoiding the computation of

*Corresponding author
Email addresses: vinicius.santos@ga.ita.br (Vinícius M. de S. Santos), tpsales@ita.br (Thiago de P. Sales), morvan.ouisse@femto-st.fr (Morvan Ouisse)

high-order evanescent modes, a task that can be difficult to perform accurately for some unit cells.

Keywords: phononic crystals, elastic metamaterials, wave-based finite element method, generalized Bloch mode synthesis, modal assurance criterion, model reduction

---

1. Introduction

Periodicity manifests in various real-life scenarios, ranging from macroscopic systems to the arrangement of atoms within a molecule. In nature, regular patterns can be found in honeycombs, forests, spider webs, snowflakes, sand dunes, pine cones, sunflower seeds, and various other situations. Additionally, several engineered systems exhibit periodicity in their design, such as airplane fuselages, railway lines, power transmission lines, pipeline systems, structural frames, heat exchanger tubes, antenna arrays, solar panels, rotating machinery blades, and numerous other instances. In the alluded scenario, a *periodic system* is defined as those structures in which a single *unit cell*, identified as the smallest repeating structure of the periodic lattice, serves as the basis for the replication of the entire structure in one, two, or three directions.

Recently, it has been demonstrated that systems properly devised, taking into account geometric and/or material periodicity, may exhibit superior properties compared to traditional designs [1–3]. In the literature, this broad class of systems is referred to as *phononic crystals* (PCs), *photonic crystals* (PhCs), or *phoxonic crystals* (PxCs), depending on the type of wave traveling through the medium. For instance, periodic systems may reveal phenomena such as waveguiding [4], cloaking [5], Anderson's localization [6], confinement [7], negative refraction index [8], non-reciprocity [9], mode conversion [10], outstanding sound absorption [11], and more.

Of great interest in structural dynamics and passive vibration reduction is the occurrence of the so-called *bandgaps*, also termed *phononic bandgaps* when they arise in PCs [12]. These bandgaps comprise frequency bands within which the propagation of various types of waves, such as elastic and acoustic, is either forbidden or strongly attenuated in space. This interesting property is attributed to the destructive interference of incident and reflected waves traveling through the periodic medium at impedance mismatches between or inside of unit cells, caused by the Bragg-scattering phenomenon

[13]. Consequently, Bragg-type bandgaps typically occur at wavelengths comparable to the order of the unit cell length [14].

Beyond Bragg-type bandgaps, forbidden bands for wave suppression can also be designed by periodically incorporating resonant devices into a host structure. In this case, the bandgap location is no longer controlled by the unit cell length but is instead determined by the resonant properties of the introduced devices, called *local resonators*. For this reason, it has been shown that bandgaps associated to the local resonance phenomenon may occur at frequency ranges much lower than those linked to Bragg-scattering [15, 16]. As examples, beam-type resonators were embedded in a host beam in [17], a periodic structure with tunable fluid-solid resonators was considered in [18], and resonators in the shape of rings were incorporated into a rotating machine in [19]. Periodic structures embedded with resonators are known as *acoustic/elastic metamaterials* (A/EMs), which can be seen as a subset of the more broad category termed *mechanical metamaterials*. Broadly speaking, PCs and A/EMs are also referred to as *metastructures*, owing to their unique properties arising from engineered periodicity or tailored material composition.

The mathematical modeling of periodic structures can be approached in various ways, including the Finite Element Method (FEM) [20, 21], Wave-based FEM (WFEM) [22, 23], Plane Wave Expansion (PWE) [24, 25], Extended PWE (EPWE) [26, 27], Spectral Element Method (SEM) [28, 29], Bloch-Floquet-based techniques [30, 31], homogenization strategies [32], and numerous other methods. Due to its versatility, the most widely adopted modeling technique is probably the FEM, which discretizes the physical domain of a structure into finite elements (FEs), enabling the analysis of its behavior through the derivation of ordinary differential equations of motion (EoMs). The FEM produces sparse matrices, speeding up calculations and reducing memory consumption. However, because of the predominantly periodic nature of PCs and A/EMs, using the FEM as a modeling strategy can be disadvantageous compared to the WFEM. By employing the WFEM, the dynamic behavior of a metastructure is investigated by analyzing a FE mesh of a single unit cell within the lattice, which considerably reduces computational time during calculations [33]. Nevertheless, challenges in runtime may still arise, especially when analyzing complex unit cells in mid- to high-frequency bands, where a fine mesh is required, leading to FE models of unit cells that can reach millions of degrees of freedom (DoFs).

A potential solution to address this issue is to use reduced-order models for unit cells, obtained through model order reduction (MOR) techniques.

This strategy has been observed in recent literature focused on computing *dispersion diagrams*, also known as *band diagrams* or *dispersion curves*, which depict the relationship between Bloch wavenumbers and frequency [34, 35]. Most of the more efficient and widely used MOR methodologies in structural dynamics are component mode synthesis (CMS)-based approaches, inspired by the seminal works published in the sixties by Hurty [36] and Craig and Bampton [37], which led to the development of the Craig-Bampton (CB) method (or Hurty-CB method). For instance, Krattiger and Hussein [30] developed an ultrafast strategy for elastic band-structure calculations called Bloch Mode Synthesis (BMS), where the interior DoFs of a unit cell of a periodic structure are represented as a set of reduced modal DoFs derived from the combination of fixed interface modes and constraint modes. A novel method for reducing the boundary DoFs of unit cells after enforcing Bloch-Floquet boundary conditions (BCs) was also introduced in [30], using system-level characteristic constraint (S-CC) interface reduction.

Four years later, Krattiger and Hussein introduced the Generalized BMS (GBMS), which mostly differs from their previous work in the sense that the reduction of boundary DoFs is performed in a single frequency-independent step before imposing the Bloch-Floquet periodicity conditions, making use of local-level characteristic constraint (L-CC) interface reduction [31]. The compatibility of boundary DoFs required for applying the Bloch-Floquet theorem after the MOR process is preserved in the GBMS, and the reduced-order models of unit cells can be employed in either the $\omega(k)$ or $k(\omega)$ methods. Krattiger and Hussein [31] also demonstrated a way to improve the CB MOR method by accounting for the influence of neglected (or residual) fixed interface modes on the unit cell's interior dynamic behavior.

In the last few years, it has been observed that the studies by Krattiger and Hussein [30, 31] have influenced subsequent research papers on the computation of dispersion curves, with several works building upon their foundational contributions. Aladwani [38] extended the BMS method to electroelastic metamaterials with piezoelectric resonant shunt damping. The BMS technique was further developed by Aladwani et al. [39] to arbitrarily damped phononic materials, resorting to the state-space formulation. Van Belle et al. [40] employed the GBMS to accelerate the calculation of dispersion curves of a two-dimensional EM. Cool et al. [41] applied the BMS and GBMS methods to compute vibro-acoustic dispersion curves of periodic structures in a solid-air medium. Xi and Zheng [34] proposed improvements to the GBMS by exploiting algebraic condensation to further accelerate dispersion curve

calculations, introducing the GBMS with algebraic condensation (GBMS-AC). Cool et al. [42] investigated the impact of the unit cell choice on the computational efficiency of band structure calculations using the GBMS. Van Belle et al. [43] used the GBMS method with substructuring to compute the forced response for a plate-type metamaterial. Zhu et al. [35] developed an Improved GBMS method, employing algebraic condensation (IGBMS-AC). Jiang et al. [44] developed a Hybrid BMS (HBMS) technique by considering a hybrid Bloch-Floquet BC for band-structure computation. More recently, Duhamel and Mencik [45] investigated time-domain responses of finite periodic structures with absorbing boundary conditions (ABCs) using unit cell reduced-order models derived as described in ref. [31], supported by standard FE assembling procedures and ABCs formulated in the wave mode space. Closely related to CMS MOR-based approaches, various Bloch-Floquet-based MOR techniques are also available in the literature to speed up the analysis of periodic structures [46, 47]. Droz et al. [48] proposed a Floquet-based model reduction method for modeling periodic structures using the WFEM under harmonic or transient loads. Wang and Amirkhizi [49] developed a reduced-order modeling approach for analyzing metamaterials constituted by beam-like elements using a limited number of simulations at selected wavevector locations.

As the developments reported so far using reduced-order models of unit cells predominantly focus on calculating dispersion curves, which are valid for analyzing wave propagation behavior in infinite periodic structures, there remains a need to explore other open-aspects of structural dynamics. In real-life, structures are not infinite, as implied by the Bloch-Floquet periodicity condition. Therefore, forced response calculations are likely the most suitable method for investigating the wave propagation characteristics of finite PCs and A/EMs. Accordingly, in this work, we propose modifications to the GBMS method derived by Krattiger and Hussein [31], allowing an efficient reduction of internal and boundary DoFs for unit cells of periodic structures, while preserving the accuracy of Bloch wavenumbers and corresponding wave modes. Such wave modes, obtained using reduced-order unit cell models, are then used in the WFEM, enabling fast and accurate computation of harmonic forced responses and related results without encountering commonly observed numerical issues, putting forward its application to more challenging problems, including those in mid- to high-frequency ranges. Although the WFEM can also be applied to investigate waveguides with local perturbations or some kind of joint or coupling elements [50–52], in this work we focus on periodic

structures, disregarding these types of features. Additionally, for the sake of simplicity, the combined use of the GBMS and the WFEM is investigated for problems encompassing one-dimensional wave propagation in this research, meaning that our interest is in the dynamic behavior of those structures where waves propagate mainly along the primary longitudinal axis. It should be noticed, nonetheless, that the proposed methodology can be extended for two- or three-dimensional wave propagation problems with suitable modifications [53–57].

The GBMS which has been used in this study differs from the technique employed by Krattiger and Hussein [31] in two main aspects: (1) Interface modes, post-processed to locally reduce boundary DoFs via L-CC MOR, are calculated for the unit cell at a global level. As a consequence, frequency-based truncation of modes has been found to be effective in delimiting the space of the lowest frequency eigenvalues obtained from the unit cell's global eigenproblem. Additionally, as the interface modes are computed considering the influence of the unit cell's internal DoFs, more reliable vibration modes for performing the reduction of boundary DoFs are obtained, as demonstrated by numerical simulations; (2) Redundant eigenmodes (i.e., those almost linearly dependent with respect to a given reference) are eliminated from the L-CC transformation matrix by exploring the well-known modal assurance criterion (MAC) index, while respecting constraints required by the periodicity condition related to the Bloch-Floquet theorem. This second modification could erroneously be taken as unnecessary; however, it addresses a critical issue. Specifically, the modal basis used to represent boundary DoFs might be assembled by discarding modes based solely on their frequency, which could be understood as the more straightforward approach and as a viable means to ensure the accuracy of the resulting unit cell reduced model. However, from another hand, this strategy does not take into account the mode shapes themselves. Consequently, redundant (almost collinear) eigenmodes may be included in the L-CC reduction matrix, unnecessarily increasing the number of retained boundary modal DoFs. In addition to reducing computational performance, such redundant modes can introduce numerical issues when computing forced responses, as demonstrated later.

The application of the WFEM considering the modified GBMS is illustrated through three examples in this work: (1) a PC composed of unit cells with inertial amplification mechanism (IAM), modeled using plane stress state assumption; (2) an EM embedded with rectangular spiral resonators, discretized with Reissner-Mindlin plate elements; (3) a PC with an internal

void with arbitrary shape, modeled using solid FEs, portraying several DoFs at the boundaries of the unit cell, disregarding the presence of fluid, such as air, in its interior, or even exterior. That is, in this work, one is interested in structural behavior, only. While vibro-acoustics should also be of interest, one will address such type of problem in a future work.

A flowchart illustrating all steps adopted by us for the ultra-fast structural dynamics analysis of periodic structures is shown in Fig. 1. In step **(1)**, the EoMs of the unit cell are obtained from the FEM, followed by spatial partitioning of DoFs into boundary and interior sets in step **(2)**. Internal DoFs are reduced through the CB MOR method in step **(3)**, employing a combination of constraint modes and fixed interface modes, while the reduction of boundary DoFs is carried out in step **(4)**, utilizing L-CC modes, which are filtered based on their frequency and according to the MAC correlation indices. Finally, the unit cell FE model with reduced interior and boundary DoFs is invoked in step **(5)**, enabling time-efficient computation of dispersion curves, harmonic deformed patterns, and other related results. It should be clarified that the term GBMS, often appearing in related literature, usually encompasses steps (**1**–**4**) in Fig. 1, as well as the computation of dispersion curves in step (**5**). However, the GBMS neither solves a global eigenproblem to reduce the boundary DoFs nor considers the MAC indices in step (**4**), which correspond to modifications introduced in this work.

To summarize the foregoing discussion, the novelties of the current work are as follows:

N1) One proposes the use of L-CC model order reduction, previously adopted to compute dispersion curves, to aid in performing structural, forced harmonic analyses of periodic structures via the WFEM; and

N2) We present modifications to the L-CC procedure, aiming to improve the reduction of boundary DoFs of a unit cell of interest. Whilst the proposed modifications might seem small, they have enabled: the utilization of a frequency-based criterion as a prior truncation metric to retain the most relevant boundary modes; the derivation of boundary modes more suitable to locally reduce the unit cells boundaries; and the elimination of numerical issues which are faced by the WFEM in structural analysis in mid- to high-frequencies.

Beyond this introduction section, this work is divided as follows: in Section 2, modeling of unit cells of periodic structures using full- and reduced-order models is introduced, followed by a review about the WFEM in Section 3.

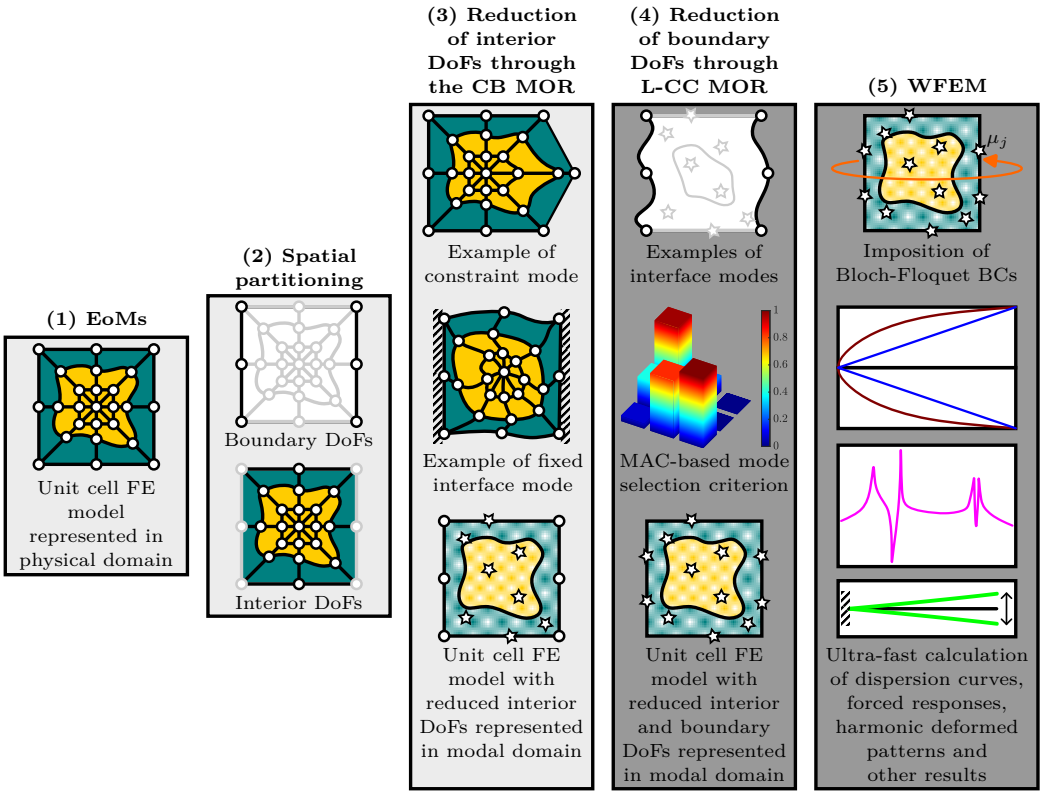

Figure 1: Flowchart depicting the various steps used for the ultra-fast analysis of periodic structures. Novelties introduced in this paper are highlighted by the darkened boxes.

Numerical experiments illustrating the application of the WFEM considering the modified/improved GBMS are presented in Section 4. The main conclusions of this work are summarized in Section 5, thereafter, acknowledgements and references are provided.

2. Full and reduced finite element models of a unit cell of periodic structures

This section presents the mathematical model of a unit cell of a periodic structure in both physical and modal (reduced) domains. First, the unit cell's EoMs, derived from FEM, are discussed in Subsection 2.1. Mathematical developments related to the reduction of interior DoFs through the CB method as developed in [30] are reviewed in Subsection 2.2. Finally, modifications

that we have made to the GBMS method outlined in [31] for unit cell MOR of boundary DoFs are introduced in Subsection 2.3.

2.1. Equations of motion of a unit cell

Figure 2, on its left, illustrates an infinite one-dimensional periodic structure formed by unit cells with inclusions of arbitrary shape. As we have chosen the FEM to discretize a unit cell's physical domain, its mesh is pictorially illustrated on the right of Fig. 2, with related DoFs and load vectors, $\hat{\mathbf{q}}$ and $\hat{\mathbf{f}}$, respectively, labeled according to left (L), internal (I), and right (R) locations.

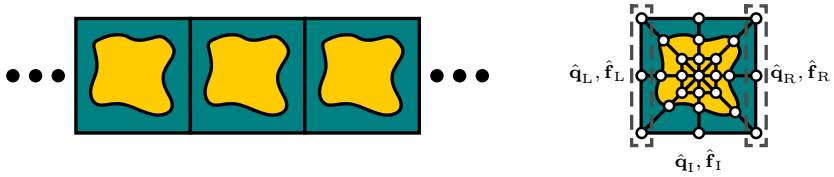

Figure 2: One-dimensional periodic structure of infinite extent, composed of unit cells containing inclusions of arbitrary shape (left) and a unit cell FE mesh with DoFs and load vectors labeled (right).

By leveraging the capabilities of conventional FE software and following step **(1)** in Fig. 1, the undamped EoMs in the time domain for a unit cell such as the one illustrated in Fig. 2 can be expressed in physical coordinates as:

$$\begin{bmatrix} \hat{\mathbf{M}}_{\mathrm{LL}} & \hat{\mathbf{M}}_{\mathrm{LR}} & \hat{\mathbf{M}}_{\mathrm{LI}} \\ \hat{\mathbf{M}}_{\mathrm{RL}} & \hat{\mathbf{M}}_{\mathrm{RR}} & \hat{\mathbf{M}}_{\mathrm{RI}} \\ \hat{\mathbf{M}}_{\mathrm{IL}} & \hat{\mathbf{M}}_{\mathrm{IR}} & \hat{\mathbf{M}}_{\mathrm{II}} \end{bmatrix} \begin{Bmatrix} \ddot{\hat{\mathbf{q}}}_{\mathrm{L}} \\ \ddot{\hat{\mathbf{q}}}_{\mathrm{R}} \\ \ddot{\hat{\mathbf{q}}}_{\mathrm{I}} \end{Bmatrix} + \begin{bmatrix} \hat{\mathbf{K}}_{\mathrm{LL}} & \hat{\mathbf{K}}_{\mathrm{LR}} & \hat{\mathbf{K}}_{\mathrm{LI}} \\ \hat{\mathbf{K}}_{\mathrm{RL}} & \hat{\mathbf{K}}_{\mathrm{RR}} & \hat{\mathbf{K}}_{\mathrm{RI}} \\ \hat{\mathbf{K}}_{\mathrm{IL}} & \hat{\mathbf{K}}_{\mathrm{IR}} & \hat{\mathbf{K}}_{\mathrm{II}} \end{bmatrix} \begin{Bmatrix} \hat{\mathbf{q}}_{\mathrm{L}} \\ \hat{\mathbf{q}}_{\mathrm{R}} \\ \hat{\mathbf{q}}_{\mathrm{I}} \end{Bmatrix} = \begin{Bmatrix} \hat{\mathbf{f}}_{\mathrm{L}} \\ \hat{\mathbf{f}}_{\mathrm{R}} \\ \hat{\mathbf{f}}_{\mathrm{I}} \end{Bmatrix}, \quad (1)$$

where $\hat{\mathbf{M}}_{ij}$ and $\hat{\mathbf{K}}_{ij}$ account for the matrices of mass and stiffness, respectively, considering the DoFs locations introduced in Fig. 2, i.e., $i, j \in \{\mathrm{L}, \mathrm{R}, \mathrm{I}\}$; $\hat{\mathbf{q}}_j$ represents time-dependent vectors of DoFs, comprising displacements and rotations in the general case; $\hat{\mathbf{f}}_j$ are the corresponding time-dependent load vectors encompassing forces and moments; and $\ddot{}$ denotes time derivatives.

In accordance with most CMS-based MOR techniques and following step **(2)** in Fig. 1, Eq. (1) is rewritten in terms of boundary (B) DoFs, encompassing those located at the unit cell's left and right interfaces (i.e., $\mathrm{B} \in \{\mathrm{L}, \mathrm{R}\}$), and internal DoFs [58]:

$$\hat{\mathbf{M}} \begin{Bmatrix} \ddot{\hat{\mathbf{q}}}_{\mathrm{B}} \\ \ddot{\hat{\mathbf{q}}}_{\mathrm{I}} \end{Bmatrix} + \hat{\mathbf{K}} \begin{Bmatrix} \hat{\mathbf{q}}_{\mathrm{B}} \\ \hat{\mathbf{q}}_{\mathrm{I}} \end{Bmatrix} = \begin{Bmatrix} \hat{\mathbf{f}}_{\mathrm{B}} \\ \hat{\mathbf{f}}_{\mathrm{I}} \end{Bmatrix}, \quad (2)$$

where:

$$\hat{\mathbf{M}} = \begin{bmatrix} \hat{\mathbf{M}}_{\mathrm{BB}} & \hat{\mathbf{M}}_{\mathrm{BI}} \\ \hat{\mathbf{M}}_{\mathrm{IB}} & \hat{\mathbf{M}}_{\mathrm{II}} \end{bmatrix}, \qquad \hat{\mathbf{K}} = \begin{bmatrix} \hat{\mathbf{K}}_{\mathrm{BB}} & \hat{\mathbf{K}}_{\mathrm{BI}} \\ \hat{\mathbf{K}}_{\mathrm{IB}} & \hat{\mathbf{K}}_{\mathrm{II}} \end{bmatrix}. \tag{3}$$

2.2. Model reduction of interior DoFs

Model reduction of interior DoFs plays a crucial role in the GBMS and WFEM, as it converts several internal DoFs represented in physical coordinates to a reduced, yet accurate, smaller number of internal modal DoFs. This procedure encompasses step **(3)** in Fig. 1, being quite important for tasks related to step **(4)** – to be discussed in Subsection 2.3 –, which involves the solution of an eigenproblem at the global level of the unit cell.

The reduction of interior DoFs of a unit cell, such as the one illustrated in Fig. 2, can be achieved through various strategies. In this work, we employ the CB MOR method, one of the most widely used MOR techniques in structural dynamics and CMS-based applications [59]. Related literature can be found in seminal works [36, 37], as well as in more recent research [30, 31], where the BMS and GBMS methods were introduced, for example. Within this MOR approach, boundary DoFs are preserved after reducing the unit cell's internal DoFs. Consequently, the Bloch-Floquet periodicity condition can be directly imposed afterward, as it would be in the absence of this MOR step. This, in turn, does not mean that $\hat{\mathbf{M}}_{\mathrm{BB}}$ and $\hat{\mathbf{K}}_{\mathrm{BB}}$ in Eq. (3) remain unchanged after reducing the interior DoFs; they are modified to account for partial influence the unit cell interior DoFs exert on its boundary DoFs. Accordingly, the following transformation holds:

$$\begin{Bmatrix} \hat{\mathbf{q}}_{\mathrm{B}} \\ \hat{\mathbf{q}}_{\mathrm{I}} \end{Bmatrix} = \mathbf{T}_{\mathrm{CB}} \begin{Bmatrix} \hat{\mathbf{q}}_{\mathrm{B}} \\ \mathbf{q}_{\mathrm{I}} \end{Bmatrix}, \tag{4}$$

where $\mathbf{q}_{\mathrm{I}}$ (without a hat) represents a set of internal modal DoFs; $\mathbf{T}_{\mathrm{CB}}$ is the CB projection matrix, given by:

$$\mathbf{T}_{\mathrm{CB}} = \begin{bmatrix} \mathbf{I} & \mathbf{0} \\ \mathbf{\Gamma} & \mathbf{\Xi} \end{bmatrix}; \tag{5}$$

$\mathbf{I}$ is an identity matrix of size $(n_{\mathrm{L}} + n_{\mathrm{R}}) \times (n_{\mathrm{L}} + n_{\mathrm{R}})$; $\mathbf{\Gamma}$ is the matrix of constraint modes of size $n_{\mathrm{I}} \times (n_{\mathrm{L}} + n_{\mathrm{R}})$; $\mathbf{\Xi}$ is the matrix of fixed interface modes of size $n_{\mathrm{I}} \times n_{\mathrm{CB}}$; n_j, for $j \in \{\mathrm{L}, \mathrm{R}, \mathrm{I}\}$, is the number of DoFs related to partitions illustrated in Fig. 2; and n_{CB} is the number of fixed interface modes, significantly smaller than n_{I} ($n_{\mathrm{CB}} \ll n_{\mathrm{I}}$).

The matrix of fixed interface modes $\boldsymbol{\Xi}$ can be assembled by first solving the eigenvalue problem resulting from Eq. (2), with all boundary DoFs constrained to be nil:

$$\left(\hat{\mathbf{K}}_{\mathrm{II}} - \kappa_j \hat{\mathbf{M}}_{\mathrm{II}}\right) \boldsymbol{\xi}_j = \mathbf{0}, \tag{6}$$

which leads to:

$$\boldsymbol{\Xi} = \begin{bmatrix} \boldsymbol{\xi}_1 & \boldsymbol{\xi}_2 & \cdots & \boldsymbol{\xi}_{n_{\mathrm{CB}}} \end{bmatrix}, \quad \text{for} \quad \kappa_j \in \{\kappa_1, \kappa_2, \ldots, \kappa_{n_{\mathrm{CB}}}\}, \tag{7}$$

where n_{CB} is determined through a frequency-based truncation criterion. Specifically, n_{CB} corresponds to the number of fixed interface modes such that $\kappa_j^{0.5}/(2\pi) \leqslant (\hat{n} \times f_{\max})$, with $\hat{n}$ representing a multiplicative factor (e.g., $\hat{n} = 1.5$, 3, 5) and $f_{\max}$ denoting the maximum frequency of analysis (in hertz). In summary, $\boldsymbol{\Xi}$ plays the role of considering the necessary information about the interior dynamics of a unit cell during the model reduction of interior DoFs, while keeping its boundary DoFs unaltered.

On the other hand, the matrix of constraint modes, $\boldsymbol{\Gamma}$, addresses the influence of the fixed (preserved) boundaries in the MOR of interior DoFs of the unit cell. It can be calculated using the Guyan method (or static reduction) [60]:

$$\boldsymbol{\Gamma} = -\hat{\mathbf{K}}_{\mathrm{II}}^{-1} \hat{\mathbf{K}}_{\mathrm{IB}}. \tag{8}$$

Computing the matrix of fixed interface, low-frequency modes ($\boldsymbol{\Xi}$) can be achieved efficiently by employing iterative solvers, such as the Arnoldi method, implemented as `eigs` in MATLAB® [61] for sparse matrices. This approach takes advantage of the sparse nature of matrices $\hat{\mathbf{K}}_{\mathrm{II}}$ and $\hat{\mathbf{M}}_{\mathrm{II}}$, potentially reducing the solution time for the eigenvalue problem in Eq. (6) from $\mathcal{O}(n^3)$ to $\mathcal{O}(n)$ — with n here denoting the number of equations involved in the calculations —, as discussed in [31]. Similarly, the computation indicated in Eq. (8) can be efficiently performed using the sparse supernodal Cholesky algorithm, which is implicitly invoked by the backslash operator of MATLAB® [61].

Based on the previously reviewed theory, the EoMs for the unit cell of a periodic structure, with internal DoFs reduced from n_{I} to n_{CB}, while preserving the boundary DoFs, can be expressed as:

$$\bar{\mathbf{M}} \begin{Bmatrix} \ddot{\hat{\mathbf{q}}}_{\mathrm{B}} \\ \ddot{\mathbf{q}}_{\mathrm{I}} \end{Bmatrix} + \bar{\mathbf{K}} \begin{Bmatrix} \hat{\mathbf{q}}_{\mathrm{B}} \\ \mathbf{q}_{\mathrm{I}} \end{Bmatrix} = \mathbf{T}_{\mathrm{CB}}^{\mathrm{T}} \begin{Bmatrix} \hat{\mathbf{f}}_{\mathrm{B}} \\ \hat{\mathbf{f}}_{\mathrm{I}} \end{Bmatrix}, \tag{9}$$

where $\bar{\mathbf{M}} = \mathbf{T}_{\text{CB}}^{\text{T}} \hat{\mathbf{M}} \mathbf{T}_{\text{CB}}$, $\bar{\mathbf{K}} = \mathbf{T}_{\text{CB}}^{\text{T}} \hat{\mathbf{K}} \mathbf{T}_{\text{CB}}$, and $^{\text{T}}$ is the transpose operator.

Note that, as discussed previously, although the boundary DoFs are preserved after performing the reduction of boundary DoFs (step (**3**) in Fig. 1), $\bar{\mathbf{M}}_{\text{BB}}$ and $\bar{\mathbf{K}}_{\text{BB}}$ in Eq. (9) write as $\bar{\mathbf{M}}_{\text{BB}} = \hat{\mathbf{M}}_{\text{BB}} + \hat{\mathbf{M}}_{\text{BI}}\boldsymbol{\Gamma} + \boldsymbol{\Gamma}^{\text{T}}\hat{\mathbf{M}}_{\text{IB}} + \boldsymbol{\Gamma}^{\text{T}}\hat{\mathbf{M}}_{\text{II}}\boldsymbol{\Gamma}$ and $\bar{\mathbf{K}}_{\text{BB}} = \hat{\mathbf{K}}_{\text{BB}} + \hat{\mathbf{K}}_{\text{BI}}\boldsymbol{\Gamma} + \boldsymbol{\Gamma}^{\text{T}}\hat{\mathbf{K}}_{\text{IB}} + \boldsymbol{\Gamma}^{\text{T}}\hat{\mathbf{K}}_{\text{II}}\boldsymbol{\Gamma}$, respectively, thus partially taking into account coupling between interior and boundary DoFs. Other coupling takes place by means of $\bar{\mathbf{M}}_{\text{BI}}$, $\bar{\mathbf{M}}_{\text{IB}}$, $\bar{\mathbf{K}}_{\text{BI}}$ and $\bar{\mathbf{K}}_{\text{IB}}$, naturally.

2.3. Model reduction of boundary (interface) DoFs

In accordance with the flowchart depicted in Fig. 1, local interface modal reduction (step **(4)**) is conducted after carrying out the reduction of internal DoFs of a unit cell, although it is not a requirement, as discussed later. Additionally, this reduction must be performed in a way that enables the subsequent application of Bloch-Floquet periodicity conditions [31]. This implies that the transformation matrix associated with the reduction of boundary DoFs must use the so-called *compatible modes*, meaning that the modal DoFs at the unit cell's left interface must necessarily be compatible with those modal DoFs at its right extremity after the reduction process is accomplished. Having this in mind, one writes:

$$\begin{Bmatrix} \hat{\mathbf{q}}_{\text{B}} \\ \mathbf{q}_{\text{I}} \end{Bmatrix} = \mathbf{T}_{\text{L-CC}} \begin{Bmatrix} \mathbf{q}_{\text{B}} \\ \mathbf{q}_{\text{I}} \end{Bmatrix}, \tag{10}$$

where:

$$\mathbf{T}_{\text{L-CC}} = \begin{bmatrix} \mathbf{L} & \mathbf{0} \\ \mathbf{0} & \mathbf{I} \end{bmatrix}, \tag{11}$$

$$\mathbf{L} = \begin{bmatrix} \boldsymbol{\Psi}_{\text{LR}} & \mathbf{0} \\ \mathbf{0} & \boldsymbol{\Psi}_{\text{LR}} \end{bmatrix}, \tag{12}$$

and:

$$\boldsymbol{\Psi}_{\text{LR}} = \begin{bmatrix} \boldsymbol{\psi}_{\text{L}} & \boldsymbol{\psi}_{\text{R}} \end{bmatrix}. \tag{13}$$

The columns of $\boldsymbol{\psi}_{\text{L}}$ and $\boldsymbol{\psi}_{\text{R}}$ in the matrix of compatible modes $\boldsymbol{\Psi}_{\text{LR}}$ above correspond to partitions of modes $\boldsymbol{\psi}_j$ that satisfy:

$$\left(\bar{\mathbf{K}} - \gamma_j \bar{\mathbf{M}}\right) \boldsymbol{\psi}_j = \mathbf{0}, \tag{14}$$

i.e.:

$$\boldsymbol{\psi}_{\mathrm{L}} = \left[(\boldsymbol{\psi}_1)_{\mathrm{L}} \quad (\boldsymbol{\psi}_2)_{\mathrm{L}} \quad \cdots \quad \left(\boldsymbol{\psi}_{n_{\text{L-CC}}}\right)_{\mathrm{L}} \right], \tag{15}$$

$$\boldsymbol{\psi}_{\mathrm{R}} = \left[(\boldsymbol{\psi}_1)_{\mathrm{R}} \quad (\boldsymbol{\psi}_2)_{\mathrm{R}} \quad \cdots \quad \left(\boldsymbol{\psi}_{n_{\text{L-CC}}}\right)_{\mathrm{R}} \right], \tag{16}$$

where $\left(\boldsymbol{\psi}_j\right)_{\mathrm{L}}$ and $\left(\boldsymbol{\psi}_j\right)_{\mathrm{R}}$ are used to indicate subsets of a given mode $\boldsymbol{\psi}_j$. The value of $n_{\text{L-CC}}$ is determined using the same frequency-based criterion employed to determine n_{CB}, presented earlier in Subsection 2.2, i.e., $n_{\text{L-CC}}$ corresponds to the number of vibration modes such that $\gamma_j^{0.5}/(2\pi) \leqslant (\bar{n} \times f_{\max})$, with $\bar{n}$ representing a multiplicative factor, not necessarily equal to $\hat{n}$.

Aiming to mitigate numerical issues arising from the MOR process and eliminate redundant modes from the L-CC projection matrix $\mathbf{T}_{\text{L-CC}}$, and consequently from the final reduced modal model, Eq. (13) can be rewritten as:

$$\boldsymbol{\Psi}_{\mathrm{LR}} = \left[\boldsymbol{\psi}_{\mathrm{L}} \quad \tilde{\boldsymbol{\psi}}_{\mathrm{R}} \right], \tag{17}$$

where $\tilde{\boldsymbol{\psi}}_{\mathrm{R}}$ is a subset of modes collected in $\boldsymbol{\psi}_{\mathrm{R}}$, corresponding to those for which the MAC index, given by [62]:

$$\mathrm{MAC}\left\{ \left(\boldsymbol{\psi}_j\right)_{\mathrm{L}}, \left(\boldsymbol{\psi}_j\right)_{\mathrm{R}} \right\} = \frac{\left| \left(\boldsymbol{\psi}_j\right)_{\mathrm{L}}^{\mathrm{T}} \left(\boldsymbol{\psi}_j\right)_{\mathrm{R}}^{*} \right|^2}{\left(\left(\boldsymbol{\psi}_j\right)_{\mathrm{L}}^{\mathrm{T}} \left(\boldsymbol{\psi}_j\right)_{\mathrm{L}}^{*} \right) \left(\left(\boldsymbol{\psi}_j\right)_{\mathrm{R}}^{\mathrm{T}} \left(\boldsymbol{\psi}_j\right)_{\mathrm{R}}^{*} \right)}, \tag{18}$$

is lower than a user-defined threshold value $\mathrm{TV}_{\mathrm{MAC}}$, with $|\ \ |$ denoting the absolute value of a scalar and * the complex conjugate operation. The number of mode partitions collected in $\tilde{\boldsymbol{\psi}}_{\mathrm{R}}$, equal to $n_{\tilde{\mathrm{R}}}$, can range from zero to at most $n_{\text{L-CC}}$. For the case when $n_{\tilde{\mathrm{R}}} = n_{\text{L-CC}}$, one obtains $\tilde{\boldsymbol{\psi}}_{\mathrm{R}} = \boldsymbol{\psi}_{\mathrm{R}}$, so that $\boldsymbol{\Psi}_{\mathrm{LR}} = [\boldsymbol{\psi}_{\mathrm{L}} \ \ \boldsymbol{\psi}_{\mathrm{R}}]$. It is important to note that, the number of modes which get collected in $\tilde{\boldsymbol{\psi}}_{\mathrm{R}}$ is inherently dependent on the unit cell dynamics, being influenced, for instance, by its degree of symmetry. More details about the selection of $\mathrm{TV}_{\mathrm{MAC}}$ and related consistent modes are provided later, in Subsections 4.1.3 and 4.3.1, respectively.

The MAC number is a measure of the degree of correlation between two eigenvectors, widely used in structural dynamics. It is bounded between 0 and 1, where values close to 0 indicate the absence of correlation between the two vectors, suggesting that they are dissimilar or unrelated. In contrast, values approaching 1 show a high degree of correlation, suggesting that the vectors are similar, or have nearly identical shapes [63]. Therefore, the MAC number can be understood as an efficient tool for removing redundant modes from

Eq. (13), as a simple frequency-based truncation criterion does not take into account mode shapes themselves. Among other problems, keeping redundant modes in Eq. (13), can (1) increase the number of equations in the reduced modal model, and (2) lead to numerical issues during the computation of forced responses and other related results in the WFEM. Additionally, note that an excessive number of boundary DoFs causes complications in the WFEM-related equations, introduced in Section 3, as the relevant expressions depend on their amount.

Last, but not least, after assembling $\boldsymbol{\Psi}_{\mathrm{LR}}$, following the procedure described above, resulting in Eq. (17), it is of utmost importance to guarantee that it is not singular, by ensuring that the partitions of vibration modes collected in $\boldsymbol{\Psi}_{\mathrm{LR}}$ (Eq. (17)) be linearly independent [64]. This task can be accomplished by orthogonalizing $\boldsymbol{\Psi}_{\mathrm{LR}}$, using, for example, singular value decomposition (SVD). The SVD of $\boldsymbol{\Psi}_{\mathrm{LR}}$ can be performed such that $\mathrm{SVD}(\boldsymbol{\Psi}_{\mathrm{LR}}) = \mathbf{U}\boldsymbol{\Sigma}\mathbf{V}^{\mathrm{T}}$, where $\mathbf{U}$ and $\mathbf{V}$ represent matrices of left and right singular vectors, respectively, and $\boldsymbol{\Sigma}$ is a diagonal matrix of singular values of $\boldsymbol{\Psi}_{\mathrm{LR}}$. If some singular values are very small, the matrix of left singular vectors given by $\mathbf{U}$ can be truncated, retaining the n_{SVD} most significant ones (where n_{SVD} denotes the number of dominant singular values), without significantly affecting the original basis $\boldsymbol{\Psi}_{\mathrm{LR}}$. Accordingly, $\boldsymbol{\Psi}_{\mathrm{LR}}$ matrix given by Eq. (17) can be rewritten as $\boldsymbol{\Psi}_{\mathrm{LR}} \rightarrow \mathbf{U}$. In MATLAB® [61], the `orth` command is a direct implementation of this procedure, meaning that $\boldsymbol{\Psi}_{\mathrm{LR}} \rightarrow \mathtt{orth}(\boldsymbol{\Psi}_{\mathrm{LR}})$. By default, the threshold value used by MATLAB® to truncate the most relevant left singular values in the `orth` command is given by $\tau = \mathtt{max}(\mathtt{size}(\boldsymbol{\Psi}_{\mathrm{LR}})) \times \mathtt{eps}(\mathtt{norm}(\boldsymbol{\Psi}_{\mathrm{LR}}))$, where `max`, `size`, `eps`, and `norm` are native functions of MATLAB®.

Therefore, the EoMs for a unit cell reduced through L-CC MOR, after its internal DoFs have been represented in modal coordinates by the CB method, can be expressed as:

$$\mathbf{M}\begin{Bmatrix}\ddot{\mathbf{q}}_{\mathrm{B}}\\ \ddot{\mathbf{q}}_{\mathrm{I}}\end{Bmatrix} + \mathbf{K}\begin{Bmatrix}\mathbf{q}_{\mathrm{B}}\\ \mathbf{q}_{\mathrm{I}}\end{Bmatrix} = \mathbf{T}_{\text{L-CC}}^{\mathrm{T}}\mathbf{T}_{\mathrm{CB}}^{\mathrm{T}}\begin{Bmatrix}\hat{\mathbf{f}}_{\mathrm{B}}\\ \hat{\mathbf{f}}_{\mathrm{I}}\end{Bmatrix}, \tag{19}$$

where $\mathbf{M} = \mathbf{T}_{\text{L-CC}}^{\mathrm{T}}\bar{\mathbf{M}}\mathbf{T}_{\text{L-CC}}$ and $\mathbf{K} = \mathbf{T}_{\text{L-CC}}^{\mathrm{T}}\bar{\mathbf{K}}\mathbf{T}_{\text{L-CC}}$. Note that, in this case, contrarily to the reduction of interior DoFs discussed previously, the L-CC projection matrix affects only the partitions of the mass and stiffness matrices related to the boundary DoFs themselves, i.e., $\mathbf{M}_{\mathrm{BB}}$ and $\mathbf{K}_{\mathrm{BB}}$ in Eq. (19) write as $\mathbf{M}_{\mathrm{BB}} = \boldsymbol{\Psi}_{\mathrm{LR}}^{\mathrm{T}}\bar{\mathbf{M}}_{\mathrm{BB}}\boldsymbol{\Psi}_{\mathrm{LR}}$ and $\mathbf{K}_{\mathrm{BB}} = \boldsymbol{\Psi}_{\mathrm{LR}}^{\mathrm{T}}\bar{\mathbf{K}}_{\mathrm{BB}}\boldsymbol{\Psi}_{\mathrm{LR}}$, respectively.

It is important to realize that the final number of equations in Eq. (19) is influenced by both the internal reduction performed by the CB method, and by the reduction of boundary DoFs through the L-CC MOR (steps **(3)** and **(4)** in Fig. 1). Therefore, it is determined by the sum $n_{\text{CB}} + (n_{\text{L-CC}} + n_{\tilde{\text{R}}})$, if $\mathbf{U}$ is not truncated, otherwise it is given by n_{CB} plus the number of relevant singular values n_{SVD}.

In general, in the proposed procedure, few modes, if any, are eliminated from $\mathbf{U}$ during the orthogonalization of $\boldsymbol{\Psi}_{\text{LR}}$, as the adopted threshold value τ is very small. In this context, SVD is used simply to avoid singularity issues that can occur if $\boldsymbol{\Psi}_{\text{LR}}$ is not orthogonalized [64].

On the other hand, SVD could also be used to discard redundant (almost collinear) modes from $\boldsymbol{\Psi}_{\text{LR}}$ [31, 45, 64]. The adoption of this strategy relies on the specification of a threshold, which may not be straightforward. It would, otherwise, eliminate the necessity of the alternative, MAC-based procedure introduced in this work. Notwithstanding, in the authors' view, the MAC-based approach is more robust than the SVD-based procedure for reducing modal boundary DoFs, as MAC indices can be used to identify and remove redundant modes from $\boldsymbol{\Psi}_{\text{LR}}$ taking directly into account spatial correlation between mode shapes. A deeper comparison of both these methods is provided in Subsection 4.4.2, considering results from numerical simulations.

Additionally, note that, instead of solving an eigenvalue problem that only considers the boundary equations for reducing the boundary DoFs, as has been done in [31, 34, 35, 40–43, 45], inhere the coupled behavior between $\mathbf{q}_{\text{I}}$ and its neighboring DoFs, collected in $\hat{\mathbf{q}}_{\text{B}}$, has been accounted for in Eq. (14). As a consequence of this modification, frequency-based truncation works very well for determining an initial modal basis for constructing $\boldsymbol{\Psi}_{\text{LR}}$, cf. Eq. (13), using the most relevant vibration modes in a given frequency band, which are afterward filtered out exploring MAC indices, leading to Eq. (17). Furthermore, this change enables the computation of more reliable boundary modes for the unit cell, improving the accuracy of the model reduction process overall, and, consequently, the computation of subsequent results, such as harmonic forced responses. This discussion is further detailed in Subsection 4.4, accompanied by comprehensive results from numerical simulations.

It must be highlighted that the proposed reduction of boundary DoFs involves the solution of a global eigenvalue problem (at the unit cell level) given by Eq. (14). Despite it involves both physical (boundaries) and modal (interior) DoFs, for the examples considered later in Section 4, the matrices $\bar{\mathbf{K}}$ and $\bar{\mathbf{M}}$ presented condition numbers similar to those found when the method

shown in [31] was used, which relies on a local eigenvalue problem, comprising physical coordinates, only. In general, the condition numbers of the previous matrices have been observed to be only slightly worse (larger) than those seen when the traditional L-CC was followed. Notwithstanding, no ill-conditioning issues were noted during the solution of Eq. (14), for the cases one studied. This is a point which deserves attention when applying the proposed method; but which would be accompanied by evident signs of issues during the solution of Eq. (14).

Lastly, it should be clarified that a single transformation matrix encompassing both the CB and L-CC MOR methods can also be derived, allowing for a straightforward expression that relates full and reduced DoFs as:

$$\begin{Bmatrix} \hat{\mathbf{q}}_{\mathrm{B}} \\ \hat{\mathbf{q}}_{\mathrm{I}} \end{Bmatrix} = \mathbf{T} \begin{Bmatrix} \mathbf{q}_{\mathrm{B}} \\ \mathbf{q}_{\mathrm{I}} \end{Bmatrix}, \tag{20}$$

where:

$$\mathbf{T} = \begin{bmatrix} \mathbf{L} & \mathbf{0} \\ \boldsymbol{\Gamma}\mathbf{L} & \boldsymbol{\Xi} \end{bmatrix}. \tag{21}$$

According to the proposed scheme for reducing the boundary DoFs, which one might cautiously term "global", $\mathbf{L}$ can be derived without the need for performing the interior reduction, because Eq. (14) is solved at the unit cell's global level, therefore considering its "complete" dynamic behavior. Of course, it is more computationally advantageous to conduct the CB MOR method before applying the L-CC MOR technique, as suggested in the flowchart depicted in Fig. 1. This approach often results in solving a much smaller eigenproblem during the L-CC model reduction step (recall that $n_{\mathrm{CB}} \ll n_{\mathrm{I}}$ was assumed in Subsection 2.2). However, it may also be the case that reduction of boundary DoFs should be performed first, which is well-supported within the proposed methodology.

On the other hand, the same cannot be achieved if the traditional methodology [31], which considers a boundary-only, "local" eigenvalue problem, is followed, as it provides eigenvectors related to blocked interior DoFs, disregarding the dynamic behavior of the unit cell as a whole. Hence, for it to work properly, the effect of interior DoFs must be taken into account on the boundaries at least statically, which is granted by the CB MOR through the matrix of constraint modes (cf. Subsection 2.2).

3. A brief review of the WFEM

This section covers the mathematical formulation of the one-dimensional WFEM using reduced-order unit cell models, corresponding to step **(5)** in Fig. 1. The explanation of the WFEM provided here is mainly a summary of findings from [65, 66] and other works duly referenced below, along with our own experiences in utilizing the method.

3.1. Basic developments

The reduced time-domain EoMs derived in the previous section, given by Eq. (19), can be reformulated in the frequency domain as $\tilde{\mathbf{D}}^{(n)}\mathbf{q}^{(n)} = \mathbf{F}^{(n)}$, where $\tilde{\mathbf{D}}^{(n)} = -\omega^2\mathbf{M} + \mathbf{K}$ represents the unit cell dynamic stiffness matrix (DSM), $\mathbf{q}^{(n)}$ and $\mathbf{F}^{(n)}$ denote frequency-dependent vectors of displacements/rotations and forces/moments, respectively. A damping model may be included in the DSM by making the unit cell's stiffness matrix complex, for example, $\mathbf{K} \to (1 + \mathrm{i}\eta)\mathbf{K}$, where η stands for the hysteretic damping coefficient [67].

Differently from the segregation of the DoFs of the unit cell performed previously for the application of MOR, i.e., in boundary and internal DoFs, a more convenient partitioning can be established for the developments related to the WFEM. This involves explicitly writing the DSM as a function of modal DoFs encountered at the unit cell's boundaries ($\mathbf{q}_{\mathrm{L}}^{(n)}$ and $\mathbf{q}_{\mathrm{R}}^{(n)}$) and internally ($\mathbf{q}_{\mathrm{I}}^{(n)}$) — according to the partitioning scheme illustrated in Fig. 2:

$$\begin{bmatrix} \tilde{\mathbf{D}}_{\mathrm{LL}}^{(n)} & \tilde{\mathbf{D}}_{\mathrm{LR}}^{(n)} & \tilde{\mathbf{D}}_{\mathrm{LI}}^{(n)} \\ \tilde{\mathbf{D}}_{\mathrm{RL}}^{(n)} & \tilde{\mathbf{D}}_{\mathrm{RR}}^{(n)} & \tilde{\mathbf{D}}_{\mathrm{RI}}^{(n)} \\ \tilde{\mathbf{D}}_{\mathrm{IL}}^{(n)} & \tilde{\mathbf{D}}_{\mathrm{IR}}^{(n)} & \tilde{\mathbf{D}}_{\mathrm{II}}^{(n)} \end{bmatrix} \begin{Bmatrix} \mathbf{q}_{\mathrm{L}}^{(n)} \\ \mathbf{q}_{\mathrm{R}}^{(n)} \\ \mathbf{q}_{\mathrm{I}}^{(n)} \end{Bmatrix} = \begin{Bmatrix} \mathbf{F}_{\mathrm{L}}^{(n)} \\ \mathbf{F}_{\mathrm{R}}^{(n)} \\ \mathbf{F}_{\mathrm{I}}^{(n)} \end{Bmatrix}. \tag{22}$$

From Eq. (22), the internal DoFs of the unit cell can be condensed to its boundaries. This step, known as dynamic condensation, does not compromise the accuracy of the unit cell's mathematical model. After dynamic condensation, it can be demonstrated how the DoFs and loads at the right side of the unit cell can be obtained from those at its left. Subsequently, by enforcing DoFs' compatibility and load equilibrium between adjacent unit cells in a periodic structure, namely (n) and $(n+1)$, i.e., $\mathbf{q}_{\mathrm{R}}^{(n)} = \mathbf{q}_{\mathrm{L}}^{(n+1)}$ and $\mathbf{F}_{\mathrm{R}}^{(n)} = -\mathbf{F}_{\mathrm{L}}^{(n+1)} + \mathbf{F}_{\mathrm{B}}^{(n)}$, where $\mathbf{F}_{\mathrm{B}}^{(n)}$ represents an external load applied to the

right interface of the n^{th} cell, the following relationship is derived [68]:

$$\mathbf{u}_{\mathrm{L}}^{(n+1)} = \mathbf{S}\mathbf{u}_{\mathrm{L}}^{(n)} + \mathbf{b}^{(n)}, \tag{23}$$

with:

$$\mathbf{u}_{\mathrm{L}}^{(n)} = \begin{Bmatrix} \mathbf{q}_{\mathrm{L}}^{(n)} \\ -\mathbf{F}_{\mathrm{L}}^{(n)} \end{Bmatrix}, \quad \mathbf{S} = \begin{bmatrix} -\mathbf{D}_{\mathrm{LR}}^{-1}\mathbf{D}_{\mathrm{LL}} & -\mathbf{D}_{\mathrm{LR}}^{-1} \\ \mathbf{D}_{\mathrm{RL}} - \mathbf{D}_{\mathrm{RR}}\mathbf{D}_{\mathrm{LR}}^{-1}\mathbf{D}_{\mathrm{LL}} & -\mathbf{D}_{\mathrm{RR}}\mathbf{D}_{\mathrm{LR}}^{-1} \end{bmatrix},$$

$$\mathbf{b}^{(n)} = \begin{Bmatrix} -\mathbf{D}_{\mathrm{LR}}^{-1}\mathbf{D}_{\mathrm{LI}}\mathbf{F}_{\mathrm{I}}^{(n)} \\ \left(\mathbf{D}_{\mathrm{RI}} - \mathbf{D}_{\mathrm{RR}}\mathbf{D}_{\mathrm{LR}}^{-1}\mathbf{D}_{\mathrm{LI}}\right)\mathbf{F}_{\mathrm{I}}^{(n)} - \mathbf{F}_{\mathrm{B}}^{(n)} \end{Bmatrix}. \tag{24}$$

In the related literature, the vector $\mathbf{u}_{\mathrm{L}}$ is known as the state vector, and $\mathbf{S}$ is recognized as the unit cell transfer matrix. The vector $\mathbf{b}$ enables one to account external loads applied at both internal and right-boundary DoFs, if they exist.

Based on the recurrence relation embedded in Eq. (23), it can be shown that:

$$\mathbf{u}_{\mathrm{L}}^{(n+1)} = \mathbf{S}^{n}\mathbf{u}_{\mathrm{L}}^{(1)} + \sum\nolimits_{k=1}^{n} \mathbf{S}^{n-k}\mathbf{b}^{(k)}, \tag{25}$$

$$\mathbf{u}_{\mathrm{L}}^{(N+1)} = \mathbf{S}^{N+1-n}\mathbf{u}_{\mathrm{L}}^{(n)} + \sum\nolimits_{k=n}^{N} \mathbf{S}^{N-k}\mathbf{b}^{(k)}, \tag{26}$$

where N represents the number of unit cells of a finite periodic structure. These expressions support mathematical developments in subsequent analyses.

3.2. Computation of wave modes

Determination of wave modes is a crucial step in the WFEM, as they form the basis for expansions used in steps which follow afterward. Additionally, the wave modes gather information related to wave shapes and dispersion characteristics, which are often calculated to investigate the dynamic behavior of periodic structures [30, 31, 34, 35, 38–44, 46–49]. This, for instance, has motivated the advances in BMS and GBMS reported previously. Unfortunately, several numerical issues may arise during this task, for reasons explained later. Therefore, this section provides the main guidelines for the efficient and accurate computation of wave modes.

As one-dimensional wave propagation phenomena are addressed in this work, the Bloch-Floquet periodicity condition for one-dimensional problems is resorted to [33]:

$$\mathbf{u}_{\mathrm{L}}^{(n+1)} = \mu\mathbf{u}_{\mathrm{L}}^{(n)}, \tag{27}$$

where $\mu = \exp(-\mathrm{i}k\Delta)$ is the propagation constant, k is the corresponding wavenumber, Δ is the unit cell length along the direction of wave propagation, and $\mathrm{i} = \sqrt{-1}$ is the unit imaginary number. If external loads are zero in Eq. (23) ($\mathbf{b}^{(n)} = \mathbf{0}$) and the Bloch-Floquet periodicity condition given by Eq. (27) is invoked, one can derive a standard eigenvalue problem as follows [69]:

$$(\mathbf{S} - \mu_j \mathbf{I})\boldsymbol{\phi}_j = \mathbf{0}. \tag{28}$$

Related solutions are the eigenpairs μ_j and $\boldsymbol{\phi}_j \propto \mathbf{u}_{\mathrm{L}}^{(n)}$ (also known as wave modes), indexed by $j \in \{1, \ldots, 2 \times (n_{\text{L-CC}} + n_{\tilde{\mathrm{R}}})\}$ (or $j \in \{1, \ldots, 2 \times n_{\text{SVD}}\}$), which store several properties related to wave propagation in infinite media. Wavenumbers, for instance, are of great interest in structural dynamics and many other areas, being computed as $k_j = (\ln \mu_j)/(-\mathrm{i}\Delta)$, to determine, for example, bandgap locations [70].

The solution of Eq. (28) might not be straightforward for many unit cell designs. As an example, this includes unit cells that have a large length along the periodicity direction, for which the computation of high-order evanescent wave modes can be challenging. In general, this happens because $\boldsymbol{\phi}_j$ collects displacements/rotations and forces/moments, whose order of magnitude can be quite disparate [71, 72]. Several formulations have been developed over the past years to improve on Eq. (28), such as the (**N**-**L**) approach, quadratic eigenvalue problem, $\mathbf{S} + \mathbf{S}^{-1}$ transformation (or Zhong's eigenvalue problem), and more [73]. In this work, the Zhong's eigenvalue problem is employed, which is a method applicable to general unit cells, symmetric or not, and is usually less prone to such numerical complications, for which the following holds [65]:

$$\left(\mathbf{A} - \lambda_j \mathbf{B}\right)\mathbf{z}_j = \mathbf{0}, \tag{29}$$

with the eigenvalues and eigenvectors of this better conditioned eigenproblem denoted as λ_j and $\mathbf{z}_j$, respectively, $\mathbf{A} = \mathbf{N}\mathbf{J}\mathbf{L}^{\mathrm{T}} + \mathbf{L}\mathbf{J}\mathbf{N}^{\mathrm{T}}$, $\mathbf{B} = \mathbf{L}\mathbf{J}\mathbf{L}^{\mathrm{T}}$, and:

$$\mathbf{N} = \begin{bmatrix} \mathbf{D}_{\mathrm{RL}} & \mathbf{0} \\ -(\mathbf{D}_{\mathrm{LL}} + \mathbf{D}_{\mathrm{RR}}) & -\mathbf{I} \end{bmatrix}, \qquad \mathbf{L} = \begin{bmatrix} \mathbf{0} & \mathbf{I} \\ \mathbf{D}_{\mathrm{LR}} & \mathbf{0} \end{bmatrix}, \qquad \mathbf{J} = \begin{bmatrix} \mathbf{0} & \mathbf{I} \\ -\mathbf{I} & \mathbf{0} \end{bmatrix}. \tag{30}$$

Since large condition numbers of $\mathbf{A}$ or $\mathbf{B}$ indicate a nearly singular problem, one can further alleviate numerical issues by employing the following methodology. If $\texttt{cond}\,(\mathbf{A}) < \texttt{cond}\,(\mathbf{B})$, where $\texttt{cond}\,(\ )$ denotes the condition number of a matrix, it is preferable to solve $(\mathbf{B} - \hat{\lambda}_j \mathbf{A})\mathbf{z}_j = \mathbf{0}$ instead of Eq.

(29) [74], whose solutions provide the inverse eigenvalues $\hat{\lambda}_j$ and corresponding eigenvectors $\mathbf{z}_j$. This means computing large eigenvalues ($\hat{\lambda}_j$) rather than small ones (λ_j) that are likely to be close to each other, a condition which could introduce numerical issues during their determination. Practice experience indicates that, before computing λ_j from $\hat{\lambda}_j$, it is strongly recommended to verify if $|\mathrm{Im}\{\hat{\lambda}_j\}| \to 0$ (e.g., less than the floating-point relative accuracy) and $|\mathrm{Im}\{\hat{\lambda}_j\}| \neq 0$. If that is the case, the approximation $\hat{\lambda}_j \approx \mathrm{Re}\{\hat{\lambda}_j\}$ can be applied, so that λ_j is recovered afterward as $\lambda_j = 1/\hat{\lambda}_j$.

As shown by Mencik and Duhamel [65], it can be demonstrated that the eigenvalues of Eq. (29) are related to each propagation constant by $\lambda_j = \mu_j + 1/\mu_j$, such that $\mu_j = \frac{1}{2}\left(\lambda_j \pm \sqrt{\lambda_j^2 - 4}\right)$. However, direct computation of μ_j employing the quadratic formula can lead to pitfalls brought by special numerical conditions, whose occurrence is not uncommon, as the terms found in the discriminant of the solution of the second-degree polynomial equation can be very disparate. This issue can also happen in the kinematics of mechanisms for determining angles between links of planar and three-dimensional systems (cf. ref. [75], p. 100). Therefore, as an alternative, μ_j can be obtained numerically by calculating the eigenvalues of the companion matrix corresponding to the polynomial equation. This algorithm is implemented in MATLAB® [61] as `roots` and satisfactorily mitigates the occurrence of numerical instabilities due to challenges in computing μ_j.

Eigenvectors of the original eigenproblem stated in Eq. (28) can be retrieved as [65]:

$$\boldsymbol{\phi}_j = \begin{bmatrix} \mathbf{I} & \mathbf{0} \\ \mathbf{D}_{\mathrm{RR}} & \mathbf{I} \end{bmatrix} \mathbf{w}_j, \qquad \text{with} \qquad \mathbf{w}_j = \mathbf{J}\left(\mathbf{L}^{\mathrm{T}} - \tfrac{1}{\mu_j}\mathbf{N}^{\mathrm{T}}\right)\mathbf{z}_j. \tag{31}$$

Eigenvalues and associated eigenvectors can be separated into those related to positive-, $(\mu_j, \boldsymbol{\phi}_j)$, and negative-going waves, $(\mu_j^*, \boldsymbol{\phi}_j^*)$, for $j \in \{1, ..., n_{\text{L-CC}} + n_{\tilde{\text{R}}}\}$ (or $j = \{1, \ldots, n_{\text{SVD}}\}$). If $|\mu_j| < 1$, the mode is associated with a wave that propagates in the positive direction; otherwise, if $|\mu_j| > 1$, the corresponding wave propagates in the negative direction. When $|\mu_j| = 1$, one can examine the power flow of the wave mode to make a decision [72, 76]. According to this assortment procedure, the following matrices can

be introduced:

$$\boldsymbol{\mu} = \mathrm{diag}(\mu_1,\ \ldots,\ \mu_{n_{\text{L-CC}}+n_{\tilde{\text{R}}}}), \quad \boldsymbol{\Phi} = \begin{bmatrix} \boldsymbol{\phi}_1 & \ldots & \boldsymbol{\phi}_{n_{\text{L-CC}}+n_{\tilde{\text{R}}}} \end{bmatrix} = \begin{bmatrix} \boldsymbol{\Phi}_{\text{q}} \\ \boldsymbol{\Phi}_{\text{F}} \end{bmatrix}, \quad (32)$$

$$\boldsymbol{\mu}^* = \mathrm{diag}(\mu_1^*,\ \ldots,\ \mu_{n_{\text{L-CC}}+n_{\tilde{\text{R}}}}^*), \quad \boldsymbol{\Phi}^* = \begin{bmatrix} \boldsymbol{\phi}_1^* & \ldots & \boldsymbol{\phi}_{n_{\text{L-CC}}+n_{\tilde{\text{R}}}}^* \end{bmatrix} = \begin{bmatrix} \boldsymbol{\Phi}_{\text{q}}^* \\ \boldsymbol{\Phi}_{\text{F}}^* \end{bmatrix}, \quad (33)$$

where subscripts q and F denote partitions of the wave modes matrices associated with displacements/rotations and forces/moments, respectively.

It should also be pointed out that, to develop expressions presented in Subsection 3.3, which rely on simplifications due to the orthogonality of wave modes, the eigenvectors collected in $\boldsymbol{\Phi}$ and $\boldsymbol{\Phi}^*$ must be normalized according to $\boldsymbol{\phi}_j \rightarrow \boldsymbol{\phi}_j(\boldsymbol{\phi}_j^{*\text{T}}\mathbf{J}\boldsymbol{\phi}_j)^{-0.5}$ and $\boldsymbol{\phi}_j^* \rightarrow \boldsymbol{\phi}_j^*(\boldsymbol{\phi}_j^{*\text{T}}\mathbf{J}\boldsymbol{\phi}_j)^{-0.5}$ [71].

3.3. Computation of harmonic forced responses

Expressions used for calculating harmonic forced responses of finite periodic systems, encompassing, for example, PCs and EMs, are briefly reviewed in this section. It should be clarified that these expressions, as well as other which have been presented throughout the work, are general, and can be applied to compute forced responses of periodic structures considering distributed or concentrated loads. They are also well suited for considering loads applied at interior and/or boundary DoFs of unit cells. The imposition of BCs is also discussed below, with the resulting expressions provided at the end. One begins by expressing the state vector, $\mathbf{u}_{\text{L}}^{(n)}$, and the vector that collects externally applied loads, $\mathbf{b}^{(n)}$, as a linear combination of wave modes' amplitudes:

$$\mathbf{u}_{\text{L}}^{(n)} = \boldsymbol{\Phi}\mathbf{Q}^{(n)} + \boldsymbol{\Phi}^*\mathbf{Q}^{*(n)}, \quad (34)$$

$$\mathbf{b}^{(n)} = \boldsymbol{\Phi}\mathbf{Q}_{\text{B}}^{(n)} + \boldsymbol{\Phi}^*\mathbf{Q}_{\text{B}}^{*(n)}, \quad (35)$$

where $\mathbf{Q}^{(n)}$, $\mathbf{Q}^{*(n)}$, $\mathbf{Q}_{\text{B}}^{(n)}$, and $\mathbf{Q}_{\text{B}}^{*(n)}$ are vectors gathering amplitudes related to the wave modes' expansion of $\mathbf{u}_{\text{L}}^{(n)}$ and $\mathbf{b}^{(n)}$. These expressions establish the connection between physical and modal (or wave mode) domains, which is the basis of the WFEM.

By manipulating Eqs. (25) and (26) in conjunction with Eqs. (34) and (35), and taking into account the orthogonality of the wave modes defined as $\boldsymbol{\Phi}^{*\text{T}}\mathbf{J}\boldsymbol{\Phi} = -\boldsymbol{\Phi}^{\text{T}}\mathbf{J}\boldsymbol{\Phi}^* = \mathbf{I}$ and $\boldsymbol{\Phi}^{\text{T}}\mathbf{J}\boldsymbol{\Phi} = \boldsymbol{\Phi}^{*\text{T}}\mathbf{J}\boldsymbol{\Phi}^* = \mathbf{0}$ [71], the following

expressions can be derived [66, 68]:

$$\mathbf{Q}^{(n)} = \boldsymbol{\mu}^{n-1}\mathbf{Q}^{(1)} + \sum\nolimits_{k=1}^{n-1} \boldsymbol{\mu}^{n-k-1}\mathbf{Q}_{\mathrm{B}}^{(k)}, \tag{36}$$

$$\mathbf{Q}^{*(n)} = \boldsymbol{\mu}^{N+1-n}\mathbf{Q}^{*(N+1)} - \sum\nolimits_{k=n}^{N} \boldsymbol{\mu}^{k-n+1}\mathbf{Q}_{\mathrm{B}}^{*(k)}, \tag{37}$$

with $\mathbf{Q}_{\mathrm{B}}^{(k)}$ and $\mathbf{Q}_{\mathrm{B}}^{*(k)}$ given by:

$$\mathbf{Q}_{\mathrm{B}}^{(k)} = \left(\boldsymbol{\mu}\boldsymbol{\Phi}_{\mathrm{q}}^{*\mathrm{T}}\mathbf{D}_{\mathrm{LI}} + \boldsymbol{\Phi}_{\mathrm{q}}^{*\mathrm{T}}\mathbf{D}_{\mathrm{RI}}\right)\mathbf{F}_{\mathrm{I}}^{(k)} - \boldsymbol{\Phi}_{\mathrm{q}}^{*\mathrm{T}}\mathbf{F}_{\mathrm{B}}^{(k)}, \tag{38}$$

$$\mathbf{Q}_{\mathrm{B}}^{*(k)} = -\left(\boldsymbol{\mu}^{*}\boldsymbol{\Phi}_{\mathrm{q}}^{\mathrm{T}}\mathbf{D}_{\mathrm{LI}} + \boldsymbol{\Phi}_{\mathrm{q}}^{\mathrm{T}}\mathbf{D}_{\mathrm{RI}}\right)\mathbf{F}_{\mathrm{I}}^{(k)} + \boldsymbol{\Phi}_{\mathrm{q}}^{\mathrm{T}}\mathbf{F}_{\mathrm{B}}^{(k)}. \tag{39}$$

Finally, combining Eqs. (34), (36), and (37), and taking into account that the state vector $\mathbf{u}_{\mathrm{L}}^{(n)}$ contains information related to DoFs and loads ($\mathbf{q}_{\mathrm{L}}^{(n)}$ and $\mathbf{F}_{\mathrm{L}}^{(n)}$, cf. Eq. (24)), along with the partitioning scheme introduced in Eqs. (32) and (33), one can show that:

$$\begin{aligned}\mathbf{q}_{\mathrm{L}}^{(n)} = {} & \boldsymbol{\Phi}_{\mathrm{q}}\boldsymbol{\mu}^{n-1}\mathbf{Q} + \boldsymbol{\Phi}_{\mathrm{q}}^{*}\boldsymbol{\mu}^{N+1-n}\mathbf{Q}^{*} \\ & + \boldsymbol{\Phi}_{\mathrm{q}}\sum\nolimits_{k=1}^{n-1}\boldsymbol{\mu}^{n-k-1}\mathbf{Q}_{\mathrm{B}}^{(k)} - \boldsymbol{\Phi}_{\mathrm{q}}^{*}\sum\nolimits_{k=n}^{N}\boldsymbol{\mu}^{k+1-n}\mathbf{Q}_{\mathrm{B}}^{*(k)}, \end{aligned} \tag{40}$$

$$\begin{aligned}-\mathbf{F}_{\mathrm{L}}^{(n)} = {} & \boldsymbol{\Phi}_{\mathrm{F}}\boldsymbol{\mu}^{n-1}\mathbf{Q} + \boldsymbol{\Phi}_{\mathrm{F}}^{*}\boldsymbol{\mu}^{N+1-n}\mathbf{Q}^{*} \\ & + \boldsymbol{\Phi}_{\mathrm{F}}\sum\nolimits_{k=1}^{n-1}\boldsymbol{\mu}^{n-k-1}\mathbf{Q}_{\mathrm{B}}^{(k)} - \boldsymbol{\Phi}_{\mathrm{F}}^{*}\sum\nolimits_{k=n}^{N}\boldsymbol{\mu}^{k+1-n}\mathbf{Q}_{\mathrm{B}}^{*(k)}, \end{aligned} \tag{41}$$

with $\mathbf{Q} \equiv \mathbf{Q}^{(1)}$ representing the wave mode amplitudes of waves that propagate from the left interface of the 1st unit cell to the right (right-going waves), and $\mathbf{Q}^{*} \equiv \mathbf{Q}^{*(N+1)}$ representing the wave mode amplitudes of waves that propagate from the right interface of the N^{th} unit cell to the left (left-going waves).

In this work, the numerical investigations presented in Section 4 have been performed considering free-free BCs, for which $\mathbf{F}_{\mathrm{L}}^{(1)} = \mathbf{0}$ and $\mathbf{F}_{\mathrm{L}}^{(N+1)} = \mathbf{0}$. The effect of external loads, in turn, was taken into account through the vector $\mathbf{F}_{\mathrm{B}}$ introduced previously, as seen later. Accordingly, resorting to the pre-conditioning procedure proposed by Mencik [33], which makes the main diagonal of coefficients matrix all ones, the following linear system of equations can be derived:

$$\begin{bmatrix} \mathbf{I} & \boldsymbol{\Phi}_{\mathrm{F}}^{-1}\boldsymbol{\Phi}_{\mathrm{F}}^{*}\boldsymbol{\mu}^{N} \\ \boldsymbol{\Phi}_{\mathrm{F}}^{*-1}\boldsymbol{\Phi}_{\mathrm{F}}\boldsymbol{\mu}^{N} & \mathbf{I} \end{bmatrix} \begin{Bmatrix} \mathbf{Q} \\ \mathbf{Q}^{*} \end{Bmatrix} = \begin{Bmatrix} \boldsymbol{\Phi}_{\mathrm{F}}^{-1}\boldsymbol{\Phi}_{\mathrm{F}}^{*}\sum_{k=1}^{N}\boldsymbol{\mu}^{k}\mathbf{Q}_{\mathrm{B}}^{*(k)} \\ -\boldsymbol{\Phi}_{\mathrm{F}}^{*-1}\boldsymbol{\Phi}_{\mathrm{F}}\sum_{k=1}^{N}\boldsymbol{\mu}^{N-k}\mathbf{Q}_{\mathrm{B}}^{(k)} \end{Bmatrix}. \tag{42}$$

Solving this system enables the determination of various responses of general periodic structures, which includes PCs or EMs, for example, in modal coordinates, by considering the expressions introduced in Eqs. (40) and (41), as well as relations embedded in Eq. (22). Physical responses can afterward be obtained by considering the relationship given by Eq. (20).

It should be noted that the size of Eq. (42) depends on the number of wave modes collected in Eqs. (32) and (33), and it is a choice that must be made during simulations. It can vary from 2 to $2 \times (n_{\text{L-CC}} + n_{\tilde{\text{R}}})$ when the reduction of boundary DoFs is performed exploring MAC indices and $\mathbf{U}$ is not truncated during the orthogonalization procedure (cf. Subsection 2.3), from 2 to $2 \times n_{\text{SVD}}$ when the reduction of boundary DoFs is performed in the same way, but left singular vectors in $\mathbf{U}$ are filtered-out during orthogonalization, or from 2 to $2 \times n_{\text{L}}$ when boundary DoFs are not reduced, i.e., are kept as physical coordinates.

4. Numerical experiments

In the subsections which follow, one illustrates the use of the GBMS together with the WFEM for conducting fast and accurate dynamic analyses of periodic structures, which may involve calculating dispersion curves, forced responses, harmonic deformed patterns, among other related results. Subsection 4.1 encompasses the investigation of a periodic structure designed by exploiting unit cells with IAM. Some numerical issues and computational challenges that ensue when full-order unit cells models are used with the WFEM are covered in Subsection 4.1.1, demonstrating one of the motivations for this work. Main guidelines for enabling a broader understanding of how to reduce internal and boundary DoFs of unit cells in periodic structures are given in Subsections 4.1.2 and 4.1.3. Afterward, the performance of the proposed modeling technique, which combines reduced-order models for unit cells with the WFEM, is investigated for an EM whose unit cells embed rectangular spiral resonators in Subsection 4.2, and for a PC characterized by a unit cell that has an internal void of arbitrary shape, and several boundary DoFs, in Subsection 4.3. Lastly, complementary results and discussions, seeking to further clarify the benefits of the proposed modeling approach and situate the current work within the state of the art, are provided in Subsection 4.4.

For all examples given below, convergence analyses were performed to assess the reliability and accuracy of the computational results in the frequency band ranging from 0 Hz to $f_{\text{max}} = 5000$ Hz, with frequency increments of 5 Hz.

The unit cell mesh was considered converged when the relative error between successive mesh refinements in the larger natural frequency of the cell, was less than 1%, as calculated by the following equation:

$$\text{Error}_{\text{mesh}} = \frac{f_{\text{coarser}} - f_{\text{finer}}}{f_{\text{finer}}}, \tag{43}$$

where f_{coarser} is the largest natural frequency calculated using the coarser mesh, and f_{finer} is the largest natural frequency calculated using the finer mesh, both smaller than $f_{\max}$ and related to the same mode.

The error between frequency response functions (FRFs) calculated using the WFEM and GBMS ($\mathbf{H}_{\text{WFEM + GBMS}}$) and the reference solution obtained by the FEM ($\mathbf{H}_{\text{FEM}}$) was quantified through two methodologies. The first one, is simply the relative error between FRFs peaks, measuring mass and stiffness variations, calculated as follows:

$$\text{RE}_{f_r j} = \frac{f_{\text{WFEM + GBMS}j} - f_{\text{FEM}j}}{f_{\text{FEM}j}}, \tag{44}$$

with $f_{\text{FEM}j}$ and $f_{\text{WFEM + GBMS}j}$ corresponding to resonance frequencies identified in the FRFs computed by the FEM and WFEM, respectively, associated to the same vibration mode. Conversely, the second error metric between FRFs, known as Cross Signature Scale Factor (CSF), measures the degree of similarity between responses in terms of amplitude. It is sensitive to damping changes and its value ranges from zero to one, operating similar to the MAC index (cf. Subsection 2.3). A value of zero means that the FRFs are completely uncorrelated, while values near one indicate a high degree of correlation or similarity between them. The CSF applied to single-input single-output systems is written as [77]:

$$\text{CSF}(\omega) = \frac{2\left|\mathbf{H}^{\text{H}}_{\text{WFEM + GBMS}}\mathbf{H}^{\text{T}}_{\text{FEM}}\right|}{\mathbf{H}^{\text{H}}_{\text{WFEM + GBMS}}\mathbf{H}^{\text{T}}_{\text{WFEM + GBMS}} + \mathbf{H}^{\text{H}}_{\text{FEM}}\mathbf{H}^{\text{T}}_{\text{FEM}}}, \tag{45}$$

where the superscript $^{\text{H}}$ denotes the Hermitian operator.

All reference FRFs shown below were obtained with finite elements, by employing the direct method (DM), as periodic structures often exhibit defect modes (whether introduced intentionally or not) that are characterized by localized vibrations [78–80] and are not adequately captured by the traditional modal superposition method. This choice, however, should not be seen as a

big challenge, as computational time remain non-prohibitive for all examples under investigation in this work. It should be clarified, nonetheless, that these reference FRFs could alternatively be calculated using a properly enriched modal superposition method, which incorporates an adequate basis enrichment procedure with residual vector calculations [81–85].

As the duration of steps involved in the performed simulations are reported later, it is clarified that they have been executed on a DELL XPS 8920 desktop computer equipped with an Intel(R) Core(TM) i7-7700 CPU running at 3.60 GHz and 32.0 GB of RAM. Additionally, our codes were developed in MATLAB® and no drastic optimizations (such as partial compilation of functions via the mex functionality) have been implemented. Routine good practices, such as pre-allocating variables, were followed, however.

4.1. Phononic crystal incorporating inertial amplification mechanism

The first problem investigated in this work is a PC composed of $N = 10$ unit cells, featuring IAM, inspired by Mizukami et al. [86]. The PC is assumed to be made of polylactic acid (PLA) with an elastic modulus of 3.5 GPa, a density of 1250 kg m^{-3}, Poisson's ratio of 0.35, and hysteretic damping of $\eta = 1\%$. Its dimensions are depicted in Fig. 3a, with $\Delta = 112$ mm. The unit cell FE model was generated using plane stress state assumptions, with the out-of-plane depth equal to 30 mm. Four- and three-noded FEs with linear interpolation functions were employed, resulting in the FE mesh shown in Fig. 3b. Specifically, this mesh was generated using a global element size

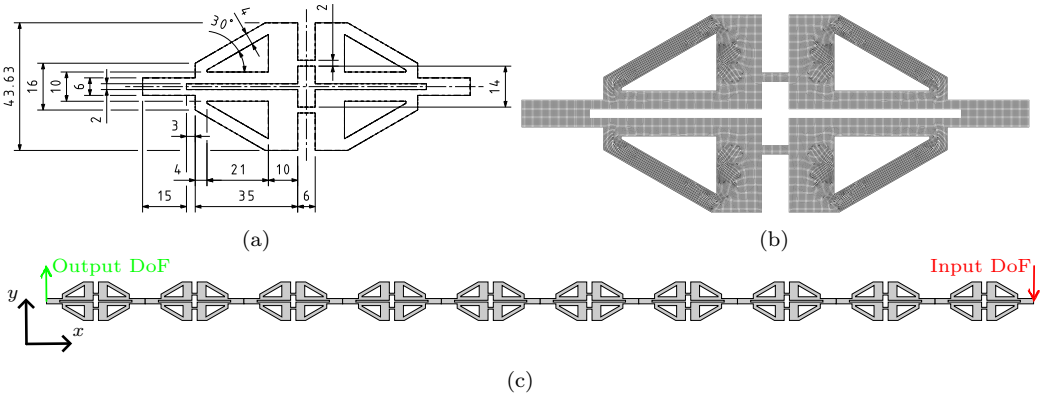

Figure 3: Phononic crystal incorporating IAM: (a) unit cell geometry and dimensions (mm), (b) its corresponding FE mesh, and (c) finite periodic structure represented along with the input and output DoFs used for computing harmonic forced responses.

of 0.25 mm, which resulted in a finite element model with 32148 nodes and 30684 elements.

All harmonic forced responses computed for the IAM-based PC in the following subsections are associated with its motion in the y-direction. Specifically, they correspond to transfer FRFs, with excitation occurring at the central node of the rightmost edge of the PC and responses obtained at its opposite side, at the leftmost edge, also at the central node of the periodic system, as shown in Fig. 3c.

4.1.1. Numerical challenges in the use of the WFEM

In this subsection, we briefly demonstrate one of the motivations for the present work. As a computational method, the WFEM is prone to several numerical issues, as illustrated by Waki et al. [72] and Mencik [71]. Beyond numerical challenges that usually arise from wrongly computed wave modes, selecting an adequate basis to convert physical DoFs and loads to the modal space is sometimes not an easy task. This preceding step is of utmost importance for forced response calculations, as they are dependent on the basis formed by the wave modes, cf., e.g., Eqs. (40) and (41). The challenges increase for dynamic analyses in higher frequency ranges, as a finer mesh is required to accurately capture the structural behavior. This, in turn, may necessitate calculating a larger number of wave modes in the WFEM to ensure proper convergence of the FRFs, leading to the involvement of large size matrices in the wave-based modeling approach.

Considering that only the internal DoFs of the IAM-based PC are reduced through the CB MOR method with a satisfactory number of fixed interface modes, equal to 38 (determined in accordance with subsequent discussion in Subsection 4.1.2), Fig. 4 shows that, when the full wave basis with 50 left-going wave modes is employed to compute the FRF, represented by the magenta solid line, numerical issues (instabilities) arise at particular frequency bands. This occurs for reasons discussed earlier in Subsection 3.2. Since the investigated PC has a unit cell length which cannot be freely modified without disturbing its overall geometry (cf. Fig. 3), the strategy proposed in [72, 73, 76] to mitigate numerical problems, consisting of reducing the length of the unit cell along the direction of wave propagation, cannot be considered.

On the other hand, if a reduced number of wave modes is employed to compute the FRF of the IAM-based PC, neglecting the highly evanescent waves for which $\mathrm{Im}(k_j) \gg \mathrm{Re}(k_j)$, $j \in \{1, 2, \ldots, 2 \times 50\}$, Fig. 4 also reveals inaccuracies near the defect modes occurring approximately at 2000 Hz and

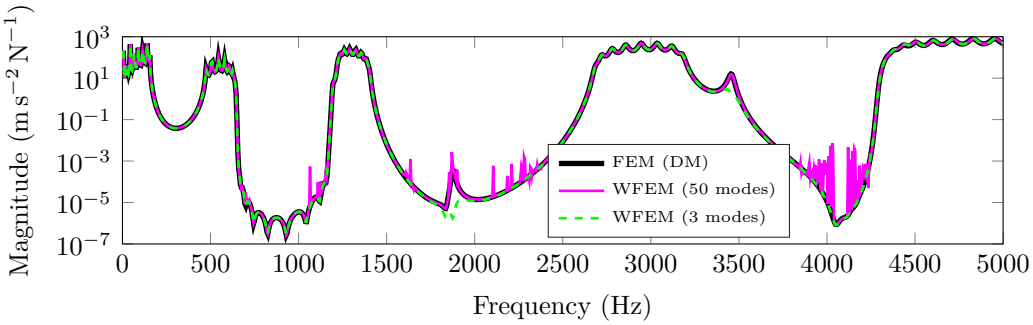

Figure 4: Comparison between the magnitude of accelerance-type FRFs obtained by the traditional FEM employing the DM and the WFEM. For the latter method, only the internal DoFs were reduced through the CB MOR method, with a converged number of fixed interface modes equal to 38 (step **(3)** in Fig. 1). Wave bases were formed by employing 50 (full wave basis) and 3 left-going wave modes. The corresponding input and output DoFs used to calculate these FRFs are shown in Fig. 3c.

3500 Hz. These inaccuracies typically occur for driving points' FRFs, for which evanescent modes are likely to influence the system's dynamics, but can also be noticed at transfer points' FRFs, as demonstrated in Fig. 4. This occurs due to the absence of certain modes in the wave mode basis, which hinders the accurate representation of localized modes, similar to what happens in the forced response computation by the traditional modal superposition-based technique, without enrichment by, e.g., residual vector(s).

Therefore, results shown in Fig. 4 illustrate the importance of considering evanescent wave modes to accurately compute FRFs of periodic structures for a particular example. The consideration of high-order evanescent modes can also be appealing in other conditions, for example, to study periodic structures embedded with defects, where wave reflection and diffraction phenomena occur at the defect locations [87]. Accordingly, in the following simulations, forced responses calculated by the WFEM were obtained using the full wave basis formed by the wave modes, whether or not reduced unit cell models have been employed. The investigation of alternative strategies to derive the wave mode basis used in the WFEM in a more efficient or optimized way is beyond the scope of this work but can be found elsewhere [47].

It should be clarified that the instabilities seen in Fig. 4 can also be mitigated by employing alternative eigenvalue problems to solve Eq. (28). Although not presented here for the sake of brevity, we found that improved accuracy of solutions can be achieved by solving the $(\mathbf{N}, \mathbf{L})$ eigenproblem

[71] instead of Zhong's eigenproblem ($\mathbf{S} + \mathbf{S}^{-1}$ approach, Eq. (29)). However, numerical issues (instabilities) still persist in some frequency bands, making the $(\mathbf{N}, \mathbf{L})$ approach unable to address all the issues seen in Fig. 4. It should be noted, however, that the $(\mathbf{N}, \mathbf{L})$ eigenproblem can only be applied to symmetric unit cells. This is the case for the cell being now considered, but the other periodic structures studied in this work all have asymmetric geometric features. Specifically, the $(\mathbf{N}, \mathbf{L})$ method is unsuitable for analyzing the EM with rectangular spiral resonators (cf. Subsection 4.2) and the PC with an internal void of arbitrary shape and several boundary DoFs (cf. Subsection 4.3). In summary, although the $(\mathbf{N}, \mathbf{L})$ eigenproblem may exhibit better stability compared to Zhong's eigenproblem, its applicability is limited to a much narrower class of structures, characterized by symmetric unit cells.

Another strategy that significantly improves the computation of forced responses by the WFEM and helps to fix instability issues is to compute the propagation constants μ_j numerically, avoiding the direct use of the quadratic formula $\left(\mu_j = \frac{1}{2}\left(\lambda_j \pm \sqrt{\lambda_j^2 - 4}\right)\right)$, cf. Subsection 3.2. This can be achieved, for example, by obtaining μ_j from the companion matrix corresponding to the polynomial equation. In MATLAB® [61], this algorithm is implemented as `roots`. To illustrate this matter, Fig. 5 shows dispersion curves (wavenumbers) obtained by directly using the quadratic formula and by applying the proposed scheme. These curves were calculated after reducing both the internal and boundary DoFs of the unit cell, using eigenvectors from the "global" eigenproblem (14) and the MAC-based approach to eliminate redundant ones from the projection basis. Considering criteria that are discussed next in Subsections 4.1.2 and 4.1.3, results were obtained using 38 fixed interface modes in the CB method (step (**3**) in Fig. 1) and 16 modes in the L-CC method (step (**4**) in Fig. 1). One clarifies that reduced-order unit cell models were employed here only to avoid handling large-scale matrices, thereby circumventing tasks demanding not-insignificant amount of time.

As can be observed in Fig. 5, the simple modification in the method used to compute the propagation constants notably improves the accuracy of results and addresses instability issues found in the traditional approach (i.e., when μ_j is computed from the quadratic formula). These instabilities in the wavenumbers k_j indicate that the propagation constants μ_j have not been computed accurately by direct application of the quadratic formula and, as a consequence, the calculation of subsequent results can be compromised. In particular, Eqs. (40) and (41), provided at the end of Subsection 3.3 and used

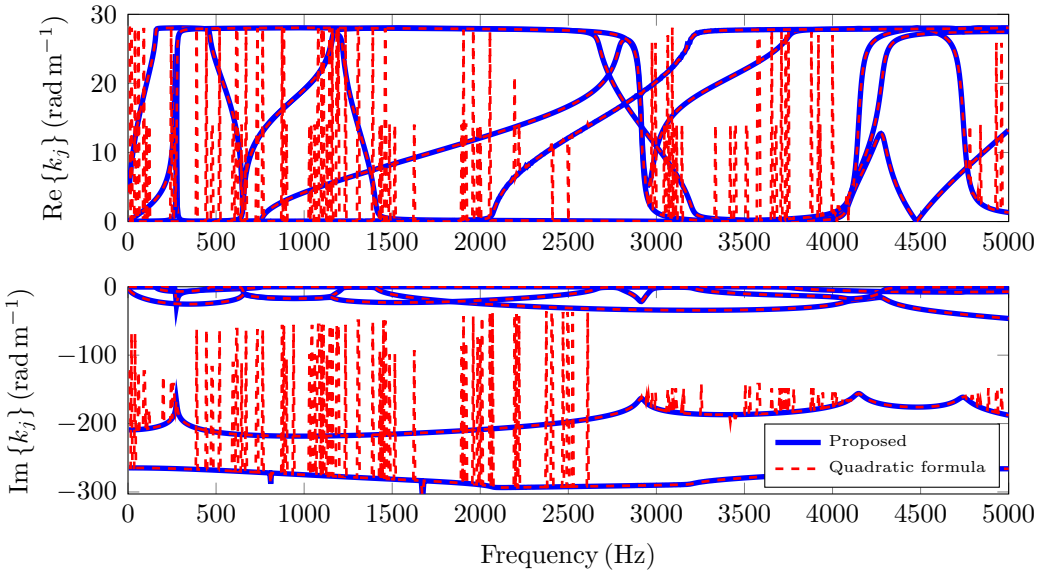

Figure 5: Dispersion curves obtained using the quadratic formula and the proposed scheme (companion matrix approach) for the calculation of propagation constants. Internal and boundary DoFs were reduced with 38 fixed interface modes considered in the CB method (step (**3**) in Fig. 1) and 16 modes in the L-CC method (step (**4**) in Fig. 1). The criteria for selecting these quantities of modes are discussed in Subsections 4.1.2 and 4.1.3.

to obtain harmonic forced responses, show that $\boldsymbol{\mu}$ can be raised to the power of N, the number of unit cells making a finite periodic structure. Specifically, terms of the form μ_j^N arise in these equations, which amplify inaccuracies present in μ_j. This leads to numerical instability and erroneous forced response predictions. The numerical computation of μ_j using the companion matrix approach avoids these issues by ensuring that the propagation constants are calculated with improved accuracy, thereby making the calculation of forced responses by the WFEM more reliable.

Lastly, it should be anticipated that the use of CB and L-CC MOR methods prior to step **(5)** in Fig. 1 is of utmost importance to guarantee numerical stability for forced response computations employing the WFEM, as well as to speed up calculations, as demonstrated later. In particular, the CB method can replace internal DoFs by a reduced, yet accurate set of modal DoFs, significantly improving subsequent operations, such as the dynamic condensation step required by the WFEM. Similarly, the L-CC MOR method enables deriving unit cell modal models with a reduced number of boundary

equations, allowing the use of full wave bases to compute forced responses in the WFEM, as needed, without encountering the numerical complications described before. In summary, by combining both MOR strategies, the dynamic behavior of general periodic structures can be efficiently assessed by the WFEM with low computational costs and minimized numerical issues. This aspect is treated in the next subsections.

4.1.2. Selection of threshold frequency used in the CB MOR method

In the literature, various threshold values $\hat{n}$ used for retaining the most relevant modes in the matrix of fixed interface modes $\boldsymbol{\Xi}$ can be found, as discussed in Subsection 2.2. However, these values are heuristics, and, owed to them, obtained reduced-order models may be inaccurate. To investigate this matter, since the CB MOR method (step **(3)**) precedes the L-CC MOR technique (step **(4)**) in the proposed methodology, as shown in Fig. 1, Fig. 6a displays the magnitude of FRFs obtained by varying the parameter $\hat{n}$, without reduction of boundary DoFs, plotted against the reference FRF calculated by FEM.

First of all, Fig. 6a reveals numerical issues in all FRFs computed using the WFEM, at the same frequency bands for which problems were seen in Fig. 4. These artificial, erroneous peaks (instabilities) are a consequence of incorrectly computing the wave basis used for obtaining the forced responses of the PC with the IAM-based unit cell, as discussed previously. In fact, full wave bases often accumulate errors, especially when unit cells with several boundary DoFs are considered. This fact emphasizes that, although a complete wave basis is relevant for investigating the dynamic behavior of periodic structures, some incorrectly computed high-order wave modes can harm the overall accuracy of responses.

Additionally, Fig. 6a also reveals that, as $\hat{n}$ increases, the magnitudes of FRFs calculated by the WFEM, with the reduction of internal DoFs, get closer to the reference result in the pass bands. Furthermore, the discrepancies between the curves, due to premature truncation of modes in the matrix of fixed interface modes, are more prominent at higher frequencies, as shown by the zoomed view in Fig. 6b. These disparities indicate that additional internal DoFs must be included in the modal model to predict the dynamic behavior of the IAM-based PC appropriately, or the effect of residual modes must be taken into account, as performed in [31]. Furthermore, Figs. 6a and 6b also show that the reduced modal models become stiffer when an insufficient number of fixed interface modes is employed in the CB MOR method. This,

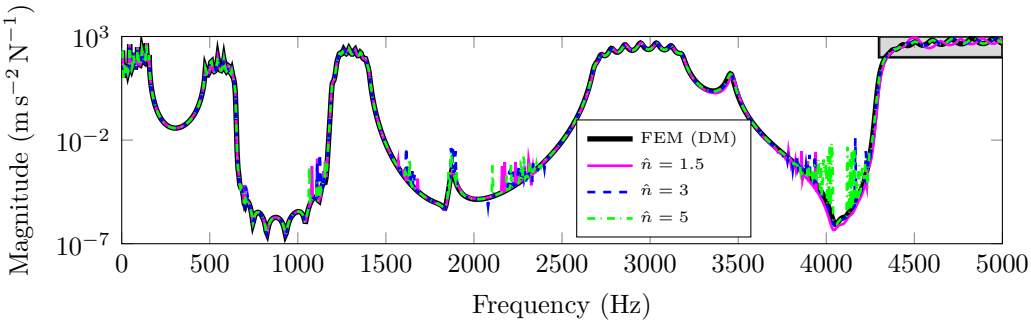

(a)

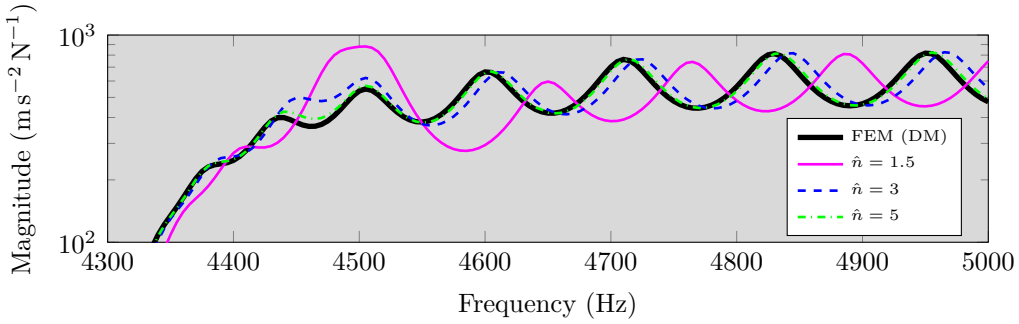

(b)

Figure 6: Comparison between the magnitudes of accelerance-type FRFs obtained by the traditional FEM employing the DM and the WFEM solely accounting for the reduction of internal DoFs. For the latter method, parametric analyses were carried out with respect to the threshold value used to determine the number of fixed interface modes, i.e., $\hat{n} = 1.5$, 3, and 5. The corresponding input and output DoFs used to calculate these FRFs are shown in Fig. 3c. (a) Complete frequency band and (b) zoomed view of higher frequencies.

for instance, often occurs when an insufficient number of normal modes is used to compute forced responses using the modal superposition method (without considering, e.g., residual vector(s)).

In the following subsections, with the aim of obtaining an accurate representation of the interior dynamics of the periodic systems under investigation, and to ensure that sources of discrepancies between the reduced and reference models are mainly related to the reduction of boundary DoFs through the L-CC method, $\hat{n}$ is set to 5. Based on Figs. 6a and 6b, this value can provide a very good match between the FRFs obtained using the reduced model and the one calculated by the FEM.

4.1.3. Selection of the threshold value used for the MAC in the L-CC MOR method

Following the steps summarized in Fig. 1, the next one consists of reducing the boundary DoFs. This task can be accomplished by following the developments shown earlier in Subsection 2.3. Accordingly, Fig. 7a depicts the magnitudes of FRFs obtained using the WFEM by varying the $\mathrm{TV_{MAC}}$ parameter, with $\hat{n}$ and $\bar{n}$ fixed as 5 and 1.2, respectively, plotted against the reference curve obtained using FEM — general discussions on the selection of $\bar{n}$ are provided in Subsection 4.4.2.

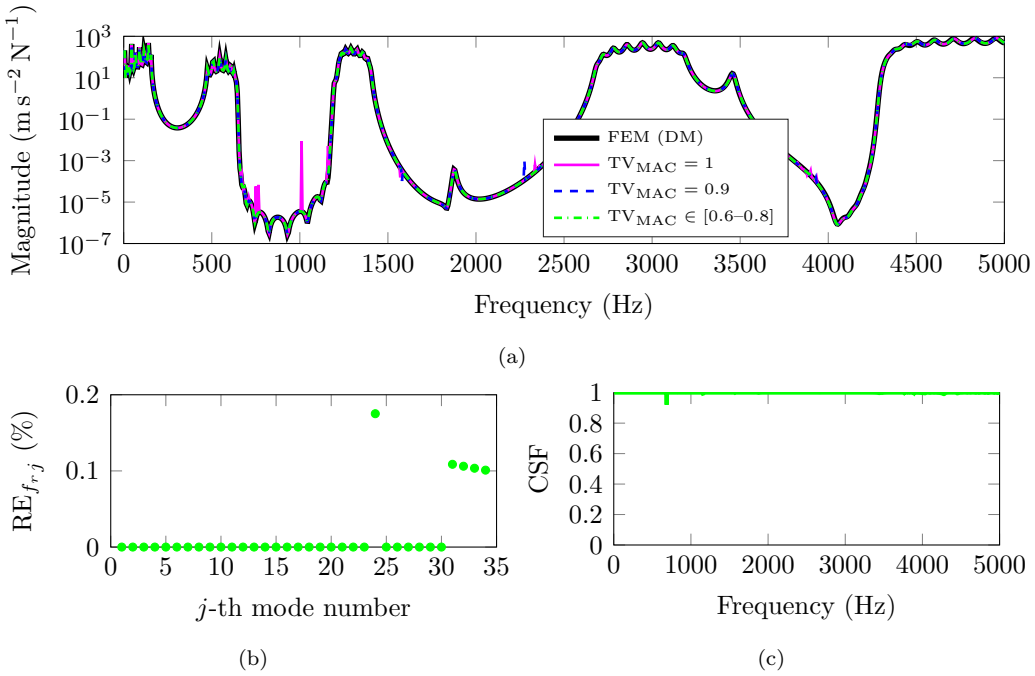

Figure 7: (a) Comparison between the magnitudes of accelerance-type FRFs obtained by the traditional FEM employing the DM and the WFEM with boundary and internal DoFs of the unit cell reduced ($\hat{n} = 5$ and $\bar{n} = 1.2$). For the latter approach, parametric analyses were carried out with respect to the threshold value used to determine the number of modes in $\tilde{\boldsymbol{\psi}}_{\mathrm{R}}$, i.e., $\mathrm{TV_{MAC}} = 1$, $\mathrm{TV_{MAC}} = 0.9$, and $\mathrm{TV_{MAC}} \in [0.6\text{–}0.8]$. The corresponding input and output DoFs used to calculate these FRFs are shown in Fig. 3c. (b) Relative error and (c) CSF between the reference curve and the one for which $\mathrm{TV_{MAC}} \in [0.6\text{–}0.8]$.

Figure 7a depicts that, when the number of partitions of vibration modes collected in $\tilde{\boldsymbol{\psi}}_{\mathrm{R}}$ corresponds to the same number of modes gathered in $\boldsymbol{\psi}_{\mathrm{L}}$, i.e., $\mathrm{TV_{MAC}} = 1$, numerical issues may still occur at some particular frequencies.

Specifically, sharp and meaningful peaks occur mainly in frequency bands at which wave propagation is highly evanescent in the FRFs, similar to what has been noticed in Figs. 4 and 6a. This can be explained by the fact that the frequency-based truncation criterion alone does not account for modal shapes, and, therefore, redundant modes can usually be inadvertently employed during the reduction of boundary DoFs. Typically, such modes are related to high-order evanescent wave modes, posing numerical challenges for their accurate calculation, often leading to issues in subsequent analyses (cf. discussions in the previous sections).

Figure 7a also reveals that, as $\mathrm{TV}_{\mathrm{MAC}}$ decreases, the responses computed by the WFEM using reduced-order unit cell models get closer to the reference curve. In fact, when $\mathrm{TV}_{\mathrm{MAC}} \in [0.6\text{–}0.8]$, the magnitudes of the FRFs computed using the WFEM perfectly superposes the reference result. Therefore, findings stemming from what is shown in Fig. 7 illustrate the importance of considering the MAC-based mode selection truncation criterion in conjunction with a frequency-based strategy, with the aim of mitigating numerical issues, and also reducing the number of equations in the final modal model. Regarding this last aspect, when $\mathrm{TV}_{\mathrm{MAC}} = 1$, Eq. (17) collects 26 vectors, whereas this number decreases to 16 for $\mathrm{TV}_{\mathrm{MAC}} \in [0.6\text{–}0.8]$. The MAC-based mode filtering criterion shows itself, therefore, as an effective strategy to remove redundant boundary modes during the reduction of boundary DoFs.

The error analysis between the reference curve and the one for which $\mathrm{TV}_{\mathrm{MAC}} \in [0.6\text{–}0.8]$ in Fig. 7a is calculated employing Eqs. (44) and (45), being depicted in Figs. 7b and 7c, respectively. The relative errors between the resonance frequencies identified by direct inspection of the magnitudes of the FRFs obtained using the reference model and the reduced one, for $\mathrm{TV}_{\mathrm{MAC}} \in [0.6\text{–}0.8]$, are negligible, with values lower than 0.2%, as observed in Fig. 7b. Similarly, the CSF model correlation index shown in Fig. 7c also indicates excellent agreement between the reduced and reference models, in terms of amplitudes, with CSF values predominantly equal to one across the entire analyzed frequency band.

Table 1 summarizes, on its left, data to assess the performance of the model reduction strategy introduced previously in Subsections 2.2 and 2.3, including the number of equations for the unit cell FE model in physical (full model) and modal (reduced model) domains. In addition, it shows, on the right, the timing data (CPU time) in seconds related to the computation of the forced responses which have been presented in Fig. 7, using the WFEM ($\hat{n} = 5$, $\bar{n} = 1.2$, and $\mathrm{TV}_{\mathrm{MAC}} \in [0.6\text{–}0.8]$) and the FEM (DM).

Table 1: Unit cell model-size details (left) and timing data (right) related to the calculation of the magnitudes of FRFs depicted in Fig. 7a using the FEM (DM) and WFEM with reduced-order unit cell models ($\mathrm{TV}_{\mathrm{MAC}} \in [0.6\text{–}0.8]$).

Unit cell model details

Set of equations	Full (N_F)	Reduced (N_R)	N_R/N_F (%)
Boundary	100	32	32
Internal	64196	38	0.06
Complete	64296	70	0.11

Timing data, presented in seconds

Step	Related equations	GBMS + WFEM	FEM (DM)
CB MOR	(4)–(9)	5.16	-
L-CC MOR	(10)–(21)	0.22	-
Computation of wave modes	(29)–(33)	3.36	-
Calculation of wave mode amplitudes	(42)	1.29	-
Post-processing: evaluation of physical DoFs	(40)–(41) (22), (20)	0.27	14044
Other	-	8.23	-
Total		18.53	14044

Table 1 clearly indicates that very small models can be obtained following the previously introduced model reduction approach. The excellent accuracy observed between the WFEM ($\mathrm{TV}_{\mathrm{MAC}} \in [0.6\text{–}0.8]$) and the reference curve in Fig. 7a is achieved with only 0.11% of equations compared to the full unit cell FEM model. Specifically, the number of equations related to boundary and internal DoFs were reduced by 32% and 0.06%, respectively.

In addition, Table 1 also shows that most of the time required for the calculation of the forced response in Fig. 7a by the WFEM ($\mathrm{TV}_{\mathrm{MAC}} \in [0.6\text{–}0.8]$) is attributed to data reading and matrix manipulations, denoted by the field "Other". One should note that this field does not comprise generation of the FE model of the unit cell, neither the export process of related matrices. The second most time-consuming task is the reduction of interior DoFs through the CB method, involving the solution of the eigenvalue problem in Eq. (6), and the algebraic system solutions required in Eq. (8), necessary to assemble the matrices of fixed interface modes $\boldsymbol{\Xi}$ and constraint modes $\boldsymbol{\Gamma}$, respectively. The computation of wave modes, $(\boldsymbol{\mu}, \boldsymbol{\Phi})$ and $(\boldsymbol{\mu}^*, \boldsymbol{\Phi}^*)$, is the next on the list. Time consumption related to this task is mainly attributed to the solution of Zhong's eigenvalue problem stated in Eq. (29) for each frequency. The remaining tasks, involving the reduction of boundary DoFs through the L-CC MOR technique, the computation of $\mathbf{Q}$ and $\mathbf{Q}^*$ using Eq. (42), and the evaluation of physical DoFs (using Eqs. (40), (41), and (22)), require negligible computational effort.

Lastly, Table 1 demonstrates that the CB and L-CC MOR methods combined with the WFEM, considerably accelerate the computation of harmonic forced responses. The analysis of the IAM-based PC using the wave-based

approach with reduced-order unit cell models reduces the time required for calculating an FRF by approximately 760 times compared to traditional FEM. Of course, this disregard some preparatory steps which are essential to run a WFEM analysis — but for which we see similar counterparts in the traditional FEM, such as model preparation and the generation of meshes.

4.2. Elastic metamaterial with rectangular spiral resonators

The second example where the strategy depicted in Fig. 1 has been applied corresponds to an EM embedded with rectangular spiral resonators, featuring $N = 10$ unit cells. The periodic system is assumed to be made of steel, for which one admits an elastic modulus of 200 GPa, density of $7850\,\mathrm{kg\,m^{-3}}$, Poisson's ratio equal to 0.3, and hysteretic damping factor $\eta = 1\%$. The dimensions of the considered unit cell are summarized in Fig. 8a, where $\Delta = 120\,\mathrm{mm}$, and a constant width of 5 mm has been assigned to the rectangular portions of the spiral. It was discretized using four-noded Reissner-Mindlin plate elements, which uses linear shape functions, having thickness of 30 mm along z. The adopted FE mesh can be seen in Fig. 8b, generated using a global element size of 1 mm, resulting in a finite element model with 9845 nodes and 9025 elements. The FRFs shown afterward have been obtained considering the input and output DoFs illustrated in Fig. 8c,

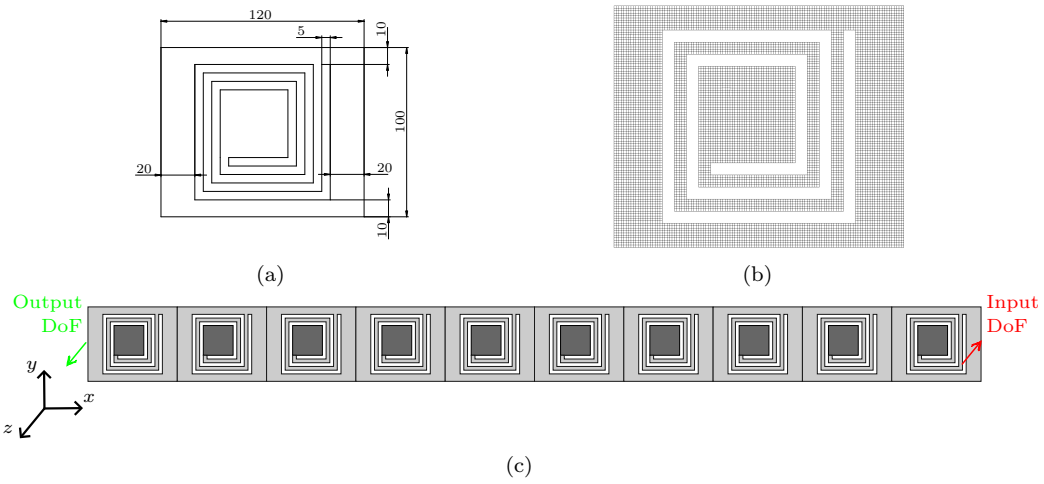

Figure 8: Elastic metamaterial with rectangular spiral resonators: (a) unit cell geometry and dimensions (mm), (b) its corresponding FE mesh, and (c) finite periodic structure represented along with the input and output DoFs used for computing harmonic forced responses.

being associated with the z-direction. The harmonic force is applied at the rightmost node of the 10^{th} unit cell, at the center of the EM, while the responses are calculated for the node situated at the leftmost edge of the periodic system, in the 1^{st} unit cell, at its midpoint.

Accordingly, Fig. 9a presents a comparison between the magnitudes of the FRFs obtained using the traditional FEM (DM) and the WFEM using unit cells' models that have boundary and internal DoFs reduced ($\hat{n} = 5$, $\bar{n} = 1.2$, and $\text{TV}_{\text{MAC}} = 0.6$). As can be observed, there is a very good correspondence between both curves. Minor discrepancies among the FRFs can be noticed at higher frequencies, where the WFEM-related curve is slightly shifted to the right. This behavior is similar to the results seen previously in Subsection 4.1.2, where the discrepancies between the reference result and those obtained by the WFEM were shown to be related to a lack of convergence in the fixed interface modes in the CB method. If it becomes necessary to improve the accuracy of the FRF obtained using the WFEM in Fig. 9a, the simplest option would be to slightly increase the value of $\bar{n}$. Alternative approaches would involve (1) increasing the TV_{MAC} parameter, or (2) considering the influence of residual modes during the reduction process as outlined in [31]. However, it should be noted that an excessive increase of $\bar{n}$ or TV_{MAC} may introduce numerical instabilities into the forced response computation, especially if the additional high-order wave modes are not adequately derived, as illustrated previously. In general, the fewer the number of boundary DoFs, the lower the chances of encountering such numerical issues. Naturally, this limited number of modal DoFs should still be sufficient to describe the system dynamics; otherwise, it will compromise the accuracy of the results.

The relative error analysis between the resonance frequencies identified from the FRFs shown in Fig. 9a is depicted in Fig. 9b, confirming minimal discrepancies between both results. Figure 9b also reveals that the deviations between the reference curve and the one obtained using the WFEM are primarily concentrated at higher frequencies, consistent with previous observations regarding Fig. 9a. In fact, the maximum relative error identified in Fig. 9b is less than 0.5%, calculated for the highest resonance frequency of the EM within the band of analysis. The CSF values shown in Fig. 9c further support these conclusions, with values close to one across the whole frequency range. Slightly lower CSF values can be observed above 3500 Hz in Fig. 9c, for specific frequencies, indicating minimal amplitude discrepancies between the FRFs obtained by the FEM and the WFEM, this latter accounting for the model reduction strategy proposed inhere.

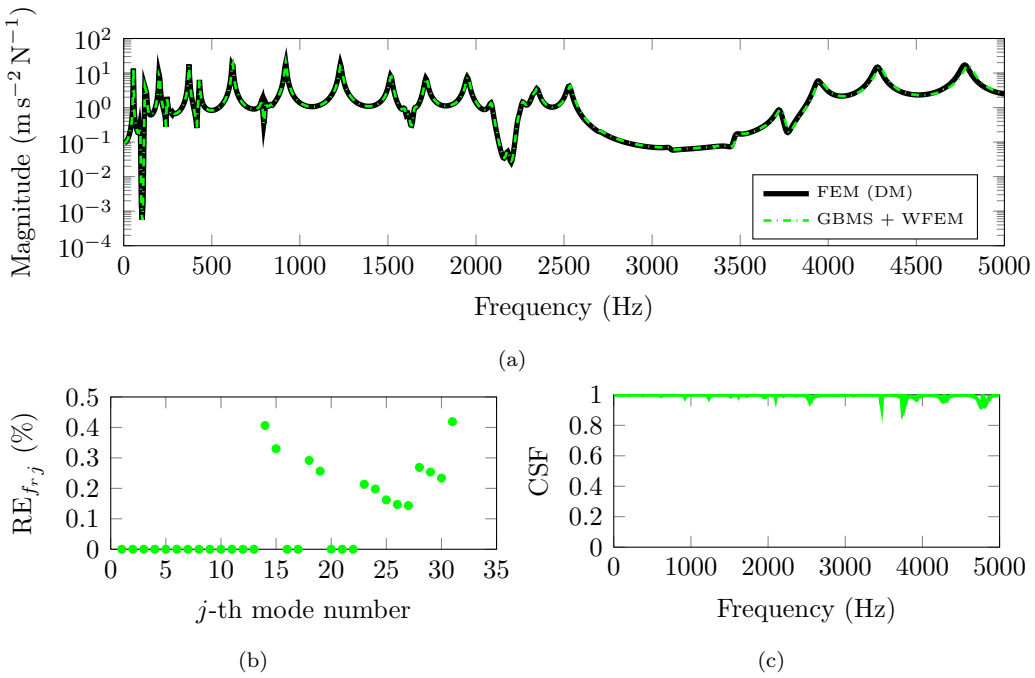

Figure 9: (a) Comparison between the magnitude of accelerance-type FRFs obtained by the traditional FEM employing the DM and the WFEM with boundary and internal DoFs of the unit cell reduced ($\hat{n} = 5$, $\bar{n} = 1.2$, and $\mathrm{TV_{MAC}} = 0.6$). The corresponding input and output DoFs used to calculate these FRFs are shown in Fig. 8c. (b) Relative error and (c) CSF between the reference curve and the one related to the WFEM.

Table 2 presents the number of equations for the EM models before and after reducing its unit cell FE model, along with a breakdown of the computational time needed for calculating the FRFs in Fig. 9a. As can be observed on the left, a significant reduction in the number of equations is achieved by reducing the unit cell FE model following the theory described earlier. The reduced modal model comprises a total number of equations equal to only 0.29% of the number of equations present in the full unit cell model, with 9.24% and 0.10% of equations observed in the internal and boundary regions, respectively.

Furthermore, Table 2 also shows that the reduced unit cell model can be used with the WFEM to calculate the magnitude of the FRF depicted in Fig. 9a 72 times faster than the traditional FEM. To perform this task, most of the computational time is spent with internal reduction of the unit cell's DoFs (step **(3)** in Fig. 1), due to relatively high number of fixed interface

Table 2: Unit cell model-size details (left) and timing data (right) related to the calculation of the magnitudes of FRFs depicted in Fig. 9a.

Unit cell model details

Set of equations	Full (N_F)	Reduced (N_R)	N_R/N_F (%)
Boundary	1212	112	9.24
Internal	57858	60	0.10
Complete	59070	172	0.29

Timing data, presented in seconds

Step	Related equations	GBMS + WFEM	FEM (DM)
CB MOR	(4)–(9)	55.98	-
L-CC MOR	(10)–(21)	6.02	-
Computation of wave modes	(29)–(33)	32.88	-
Calculation of wave mode amplitudes	(42)	14.27	-
Post-processing: evaluation of physical DoFs	(40)–(41) (22), (20)	0.92	8455
Other	-	7.48	-
Total		117.55	8455

modes needed to assemble $\boldsymbol{\Xi}$, as a result of several resonance frequencies of the rectangular spiral-like resonator (due to its low out-of-plane stiffness), and the calculation of $\boldsymbol{\Gamma}$ via Eq. (8). The remaining time required for each task reported in Table 2 is proportionally comparable to the time needed for performing the analysis of the IAM-based PC, cf. Table 1. Interestingly, the evaluation of the response related to the physical DoF of interest (output) took only 0.92 s, for 1000 frequency values. This provides a promising outlook with regard to obtaining an harmonic deformation pattern of the complete EM, since one would need to evaluate a maximum of $N \times 59070 = 590700$ responses, related to the physical DoFs of the structure. This would require approximately $0.92/1000 \times 590700 \approx 540$ s to obtain a deformation pattern related to a given frequency.

4.3. Phononic crystal with an internal void of arbitrary shape and several boundary DoFs

The last periodic system for which the procedures illustrated in Fig. 1 are exemplified corresponds to a PC with $N = 10$ unit cells, each one portraying an internal void of arbitrary shape. This structure is particularly interesting for investigation, as it exhibits several boundary DoFs, which poses challenges when applying the WFEM if adequate MOR is not considered. At this time, one should clarify one does not consider the presence of a fluid inside the internal void of the unit cell, i.e., the void can be thought of comprising a vacuum, but without consideration of eventual pressure gradients which would ensue from such hypothesis. Also, the unit cell is assumed to be made of PLA, with the same material properties reported in Subsection 4.1.

Relevant dimensions of the cell are provided in Fig. 10a, without detailing

the arbitrarily chosen dimensions of the hole for the sake of simplicity. In fact, this shape was generated using splines passing through a set of 33 control points. Additionally, a thickness (along z) of 20 mm was assigned to the unit cell. The PC was modeled using solid FEs with three DoFs per node, which use linear shape functions. The corresponding mesh comprises a combination of 8-node hexahedrons and 4-node tetrahedrons, as illustrated in Fig. 10b. This mesh was generated using a global element size of 1.5 mm, resulting in a finite element model with 34440 nodes and 28574 elements. Lastly, Fig. 10c schematizes the input and output DoFs, along the z-direction, used to compute the FRFs provided in what follows. The harmonic excitation location is at the 10^{th} unit cell, at the rightmost node located at the bottom corner of the periodic system, while the response is calculated for the opposite corner, located at the 1^{st} unit cell, at the leftmost node on the top of the PC.

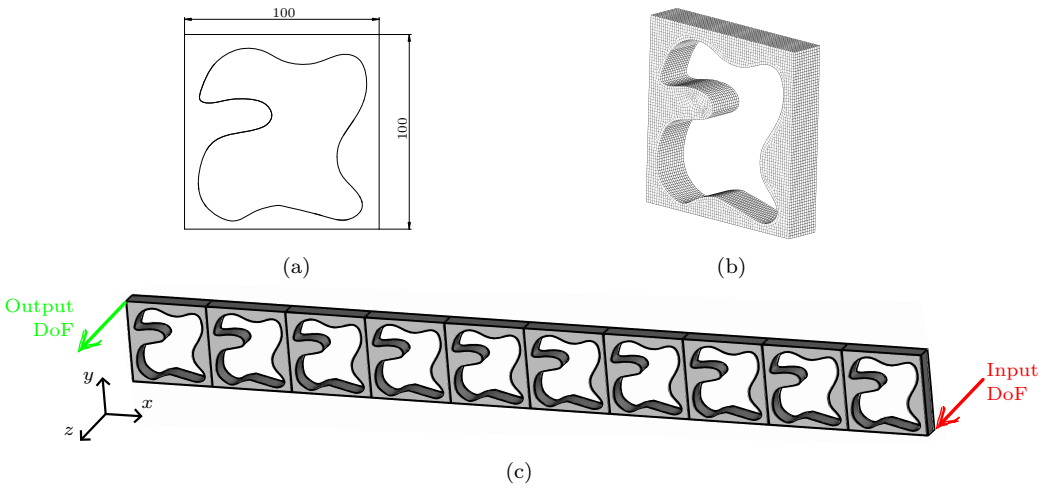

Figure 10: Phononic crystal with an internal void of arbitrary shape: (a) unit cell geometry and dimensions (mm), (b) its corresponding FE mesh, and (c) finite periodic structure represented along with the input and output DoFs used for computing harmonic forced responses.

In accordance with these aspects, Fig. 11a shows a comparison between the magnitudes of FRFs obtained by the FEM (DM) and the WFEM with reduced-order unit cell models ($\hat{n} = 5$, $\bar{n} = 1.2$, and $\text{TV}_{\text{MAC}} = 0.6$). As one may observe, a very good agreement exists between the curve obtained by the reference model and the one calculated by resorting to the wave-based propagation approach. A small frequency shift between the curves in Fig. 11a

can be noticed at higher frequencies, mainly as a consequence of neglecting high-order modes during the reduction of boundary DoFs employing the L-CC MOR, resembling findings reported previously in Subsection 4.2 and the results related to the absence of convergence of fixed interface modes in the CB method in Subsection 4.1.2.

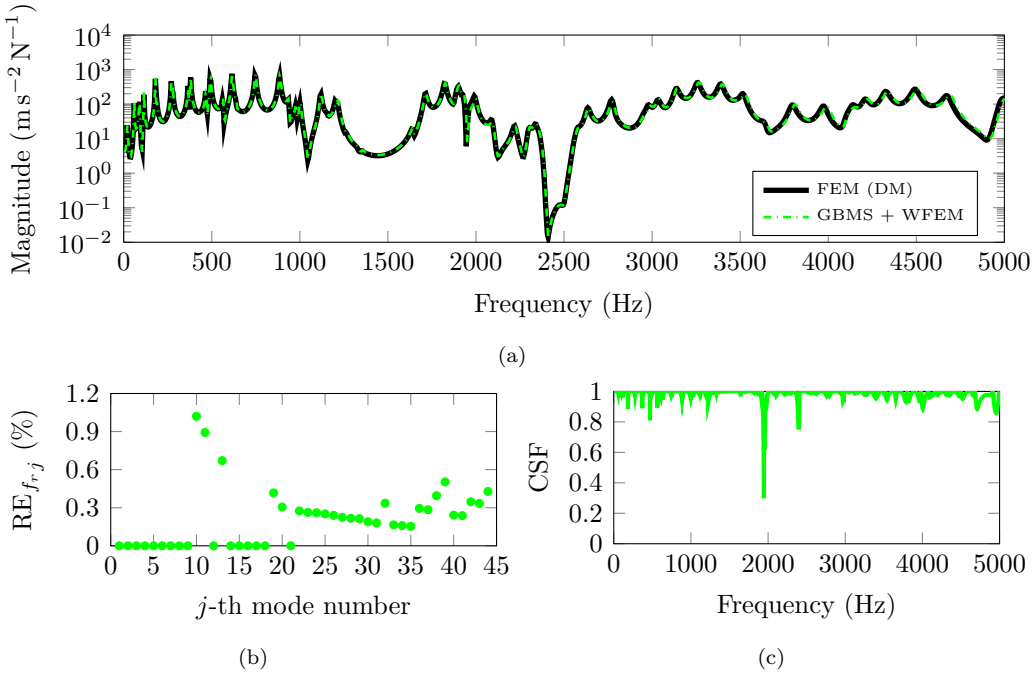

Figure 11: (a) Comparison between the magnitudes of accelerance-type FRFs obtained by the traditional FEM employing the DM and the WFEM with boundary and internal DoFs of the unit cell reduced ($\hat{n} = 5$, $\bar{n} = 1.2$, and $\text{TV}_{\text{MAC}} = 0.6$). The corresponding input and output DoFs used to calculate these FRFs are shown in Fig. 10c. (b) Relative error and (c) CSF between the reference curve and the one related to the WFEM.

The error analysis between the responses depicted in Fig. 11a, obtained using the FEM and WFEM, can be found in Figs. 11b and 11c. Firstly, Fig. 11b shows that the maximum relative error between the resonance frequencies identified from the curves shown in Fig. 11a is less than 1.2%. The maximum relative error occurs for the 10$^{\text{th}}$ resonance frequency, being mainly attributed to the frequency discretization with increments of 5 Hz we employed — i.e., smaller increments could improve the accuracy of results by providing finer resolution around the resonance peaks. In general, for lower frequencies, the relative error between resonance frequencies is zero, whereas it tends to be

more prominent for higher-order modes. In terms of amplitude, Fig. 11c shows that the CSF is virtually larger than 0.9 throughout the whole frequency band, which confirms the good amplitude match between the forced responses depicted in Fig. 11a.

The number of equations in physical and modal domains of the unit cell, and CPU time needed for calculating the FRFs shown in Fig. 11a, are summarized in Table 3. As one may observe, 97200 internal equations and 6120 boundary ones are reduced to only 54 and 86, respectively. Furthermore, a reduced modal model with only 0.13% of equations in comparison with the physical model was obtained following the model reduction methodology illustrated by steps **(3)** and **(4)** in Fig. 1.

Table 3: Unit cell model-size details (left) and timing data (right) related to the calculation of the magnitudes of FRFs depicted in Fig. 11a.

Unit cell model details

Set of equations	Full (N_F)	Reduced (N_R)	N_R/N_F (%)
Boundary	6120	86	1.40
Internal	97200	54	0.05
Complete	103320	140	0.13

Timing data, presented in seconds

Step	Related equations	GBMS + WFEM	FEM (DM)
CB MOR	(4)–(9)	4195.28	-
L-CC MOR	(10)–(21)	236.82	-
Computation of wave modes	(29)–(33)	15.39	-
Calculation of wave mode amplitudes	(42)	7.10	-
Post-processing: evaluation of physical DoFs	(40)–(41) (22), (20)	0.96	25234
Other	-	40.72	-
Total		4496.27	25234

In addition, Table 3 also shows that most of the computational time related to the calculation of the forced responses seen in Fig. 11a is attributed to the reduction of internal DoFs, similarly to what has been reported before in Table 2, for the EM with rectangular spiral resonators. For the system considered now, this occurs due to the high number of internal equations in its unit cell model (almost twice the number of internal equations of the EM), which makes the solution of Eqs. (6) and (8) slower. Table 3 additionally clarifies that the reduction of boundary DoFs was the second most time-consuming task, as the PC has a substantial number of boundary DoFs, which increases the dimensionality of Eq. (14). Time needed for data reading and matrix manipulation ranked third. Remaining tasks, including the computation of wave modes, calculation of wave mode amplitudes, and evaluation of the forced response, exhibited negligible computational cost compared to the other operations.

In the present case, employing the reduction steps introduced in Subsec-

tions 2.2 and 2.3 prior to invoking the WFEM speeds up the computation of harmonic forced responses by around 6 times. This reduction rate is not as high as the rates reported in Subsections 4.1 and 4.2, which are related to the unit cells portraying IAM and local resonators, of 760 and 72 times, respectively. This is attributed to the high number of internal DoFs found in the PC model, which leads to challenges in applying the CB MOR method, as we have just discussed. Improvements in this matter could be achieved by resorting to algebraic condensation, as reported in [34, 35]. Notwithstanding, it should be noted that, as the number of unit cells of a finite structure increases, the computational efficiency of WFEM becomes even more pronounced, due to its capability of handling large-scale periodic systems, and the high performance of the developed model reduction approach.

Lastly, it should be highlighted that no numerical issues have been identified in the computation of the forced response in Fig. 11a by the WFEM, nor in Fig. 9a. As discussed previously, by reducing the internal and boundary DoFs of a unit cell, one avoids handling large-size models, which not only decreases the computational cost during calculations but also reduces the risk of numerical instabilities such as those seen in Figs. 4, 6, and 7, for example. Therefore, in general, it is often preferable to work with smaller and simpler models, provided that they accurately capture the dynamics of interest. On the other hand, it should also be noted that the use of size-reduced unit cell models is mandatory for investigating the problems considered in this work by the WFEM, otherwise, prohibitive computational costs and memory requirements would result. Actually, the full-order unit cell models would make the analysis over the considered frequency range infeasible for the WFEM, rendering the method impractical for such structures.

4.3.1. On the selection of consistent modes in Eq. (17) *by the MAC indices*

In this subsection, one aims to elucidate the use of Eq. (18) to obtain the partitions of vibration modes which get collected in $\tilde{\boldsymbol{\psi}}_{\mathrm{R}}$ (cf. Eq. (17)). Accordingly, Fig. 12 shows the MAC indices calculated between $\boldsymbol{\psi}_{\mathrm{L}}$ and $\boldsymbol{\psi}_{\mathrm{R}}$ (cf. Eqs. (13), (15) and (16)) for the unit cell related to the PC with an internal void of arbitrary shape.

As one may observe in Fig. 12, some partitions of eigenvectors collected in $\boldsymbol{\psi}_{\mathrm{L}}$ are very close to the vibration shapes of the unit cell at its right side, gathered in $\boldsymbol{\psi}_{\mathrm{R}}$, corresponding to the MAC numbers close to 1 in the main diagonal of the bar chart. As discussed before, in Subsections 2.3 and 4.1.3, keeping similar vibration modes partition pairs in Eq. (13) is understood by

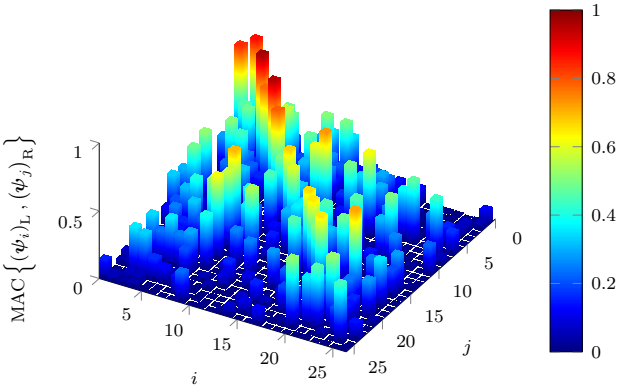

Figure 12: Bar chart illustrating the MAC indices between the partitions of vibration modes collected in $\boldsymbol{\psi}_\mathrm{L}$ and $\boldsymbol{\psi}_\mathrm{R}$ for the unit cell related to the PC with an internal void of arbitrary shape.

us to not correspond to the best practice, as they might cause numerical issues when computing forced responses, as demonstrated in Fig. 7a. Therefore, redundant modes can be removed from the set of mode partitions in $\boldsymbol{\psi}_\mathrm{R}$, so that Eq. (17) holds. Naturally, this task requires the definition of a threshold value for the MAC, as it determines which mode pairs are sufficiently similar to be considered redundant. It is important to mention that Eq. (17) can also be cast in an alternative form, as $\boldsymbol{\Psi}_\mathrm{LR} = \begin{bmatrix}\tilde{\boldsymbol{\psi}}_\mathrm{L} & \boldsymbol{\psi}_\mathrm{R}\end{bmatrix}$, where the partitions of vibration modes collected in $\boldsymbol{\psi}_\mathrm{R}$ are fully retained in the transformation matrix, and $\boldsymbol{\psi}_\mathrm{L}$ gets filtered out in an analogous fashion.

Figure 12 also depicts that most of the left and right partitions of vibration modes collected in $\boldsymbol{\psi}_\mathrm{L}$ and $\boldsymbol{\psi}_\mathrm{R}$ are rather different, as a result of small values of MAC numbers found in the main diagonal of the bar chart. For such cases, the partitions of vibration modes are dissimilar or unrelated, and therefore, they must be kept in $\boldsymbol{\Psi}_\mathrm{LR}$ to guarantee proper representation of the unit cell interfaces' dynamic behavior after performing the model reduction. It should be pointed out that, for the periodic structure being considered now, few partitions of vibration modes become neglected in the MAC-based mode selection procedure due to the asymmetry of the underlying unit cell (cf. Figs. 10a and 10b). This means that $\boldsymbol{\Psi}_\mathrm{LR}$ must be assembled with several mode shapes from both the left and right interfaces of the unit cell. However, this is not true for the IAM-based PC and EM investigated in Subsections 4.1 and 4.2. For the unit cells related to these periodic structures, several modes at the left interface of the unit cell are very similar to those at its right interface,

as can be seen from MAC indices shown in Fig. 13. As a consequence, many partitions of vibration modes can be omitted from $\boldsymbol{\Psi}_{\mathrm{LR}}$ in Eq. (17) without compromising the representation of the interface dynamics, leading to a more efficient reduced model. Therefore, the utilization of the MAC-based mode filtering procedure is very important for performing the reduction of boundary DoFs, as it reduces the number of equations in $\boldsymbol{\Psi}_{\mathrm{LR}}$. It is worth noting that, in the traditional reduction of boundary DoFs, which employs Eq. (13), with $\boldsymbol{\psi}_{\mathrm{L}}$ and $\boldsymbol{\psi}_{\mathrm{R}}$ computed locally, the number of modal boundary DoFs is doubled to satisfy the Bloch-Floquet periodicity condition [31] — an approach that is not as efficient as the method introduced in this work.

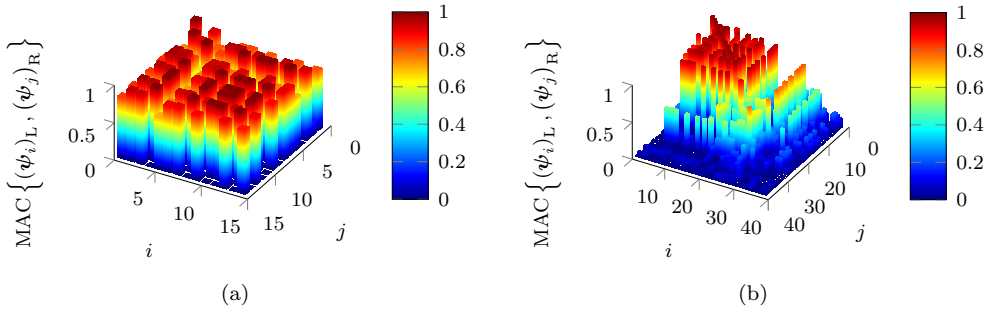

Figure 13: Bar chart illustrating the MAC indices between the partitions of vibration modes collected in $\boldsymbol{\psi}_{\mathrm{L}}$ and $\boldsymbol{\psi}_{\mathrm{R}}$ for the unit cells that incorporate (a) IAM and (b) resonators with rectangular spirals.

Lastly, Fig. 14 shows two sets of eigenvectors related to the motion of the boundaries of the unit cell with an interval void of arbitrary shape, normalized for better visualization, for two scenarios: (1) a condition where $(\boldsymbol{\psi}_{21})_{\mathrm{L}}$ is completely different from $(\boldsymbol{\psi}_{21})_{\mathrm{R}}$, as demonstrated by the shape of the modes and the MAC index value of 0.07; and (2) a situation where $(\boldsymbol{\psi}_{9})_{\mathrm{L}}$ is nearly identical to $(\boldsymbol{\psi}_{9})_{\mathrm{R}}$, clearly evidenced by their modal shapes and the MAC number of 0.79. These results illustrate the adequacy of utilizing the MAC-based mode selection procedure in conjunction with the traditional frequency-based criterion for reducing the boundary DoFs of the unit cell of a periodic structure. A boundary (interface) mode with high spatial similarity to another one should, accordingly, be removed from the projection basis, as it can be understood as almost collinear with its companion. As discussed before, this strategy is able to mitigate numerical issues that may occur in the WFEM and reduces the number of redundant equations in modal models, while respecting the constraints imposed by the periodicity conditions of the

Bloch-Floquet theorem.

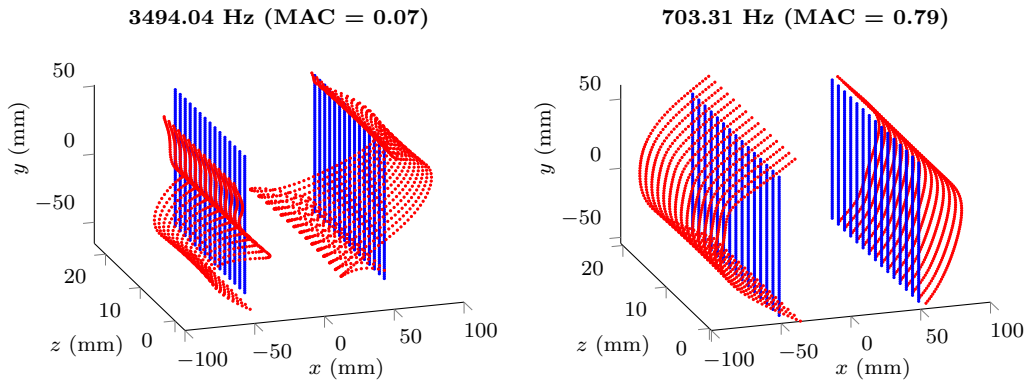

Figure 14: Eigenvectors related to the motion of the boundaries of the unit cell with an interval void of arbitrary shape (cf. Fig. 10b) for two distinct eigenvalues/frequencies. On the left, a condition where the eigenvector at the left interface is unrelated to itself at the right side; and, on the right, a situation of reasonably large spatial similarity between them.

4.4. Complementary results and discussions

In this subsection, one aims to better situate the methodologies proposed in this work with respect to the state of the art. First, in Subsection 4.4.1, the reduction of boundary DoFs using the proposed model-order reduction technique is compared with the approach currently reported in literature, by computing harmonic forced responses. The pros and cons of both approaches are discussed and clarified with numerical simulations. Then, in Subsection 4.4.2, the truncation of boundary modes using MAC- and SVD-based procedures are discussed.

4.4.1. Comparing the proposed (global) and local approaches for the reduction of boundary DoFs

The reduction of boundary DoFs using L-CC is often performed by solving an eigenvalue problem related to the boundary DoFs of the unit cell, i.e., at a local-level [31, 34, 35, 40–43, 45]. In this setting, instead of the global eigenvalue problem in Eq. (14), one has to consider:

$$\left(\bar{\mathbf{K}}_{\mathrm{BB}} - \varsigma_j \bar{\mathbf{M}}_{\mathrm{BB}}\right) \boldsymbol{\Upsilon}_j = \mathbf{0}, \tag{46}$$

where ς_j and $\boldsymbol{\Upsilon}_j = \left\{ (\boldsymbol{\Upsilon}_j)_{\mathrm{L}}^{\mathrm{T}} \;\; (\boldsymbol{\Upsilon}_j)_{\mathrm{R}}^{\mathrm{T}} \right\}^{\mathrm{T}}$, for $j \in \{1, \ldots, n_{\mathrm{L}} + n_{\mathrm{R}}\}$, are the eigenvalues and eigenvectors associated with the local eigenproblem, respectively. In light of this, Eqs. (15) and (16) should be considered taking into account the eigenvectors resulting from the solution of Eq. (46).

The related literature shows that, when the L-CC approach is used with eigenvectors of local-level eigenproblems, frequency-based truncation criterion can fail for the selection of the most-relevant, low-frequency modes in $\boldsymbol{\psi}_{\mathrm{L}}$ and $\boldsymbol{\psi}_{\mathrm{R}}$. Then, grouping the selected modes into Eq. (13) provides a "sub-optimal" basis to perform the reduction of boundary DoFs. To alleviate this issue, various mode selection strategies have been proposed in the literature, such as: 1) assuming extended, non-clearly defined frequency-based truncation criteria; 2) calculating response sensitivities due to boundary modes; 3) implementing iterative routines to verify response convergence as the number of boundary modes increases; 4) assuming a relationship between the number of boundary modes and the number of interior modal DoFs, based on a given criterion; or, 5) employing trial-and-error approaches. Although these techniques can be useful, their application generally requires careful consideration, typically involving additional steps for the reduction of boundary DoFs. In view of these aspects, an alternative approach has been proposed to perform the reduction of boundary DoFs in this work (cf. Subsection 2.3 and previously shown results), seeking to improve the mode selection procedure and to enhance the overall accuracy of the reduction process, in comparison to existing techniques.

To further investigate this matter, Fig. 15 presents FRFs calculated for each periodic structure previously analyzed in Subsections 4.1, 4.2, and 4.3, considering both the proposed (global) approach (with results from Figs. 7a, 9a, and 11a repeated for convenience) and the local method currently reported in the literature, alongside reference FRFs obtained with the FEM. For the calculation of FRFs using the local approach, most parameters were chosen equal to those used for the global method, i.e., $\hat{n} = 5$ and $\bar{n} = 1.2$. Notwithstanding, the rank of $\boldsymbol{\Psi}_{\mathrm{LR}} = [\boldsymbol{\psi}_{\mathrm{L}} \;\; \boldsymbol{\psi}_{\mathrm{R}}]$ is commonly reduced based on its SVD ($\boldsymbol{\Psi}_{\mathrm{LR}} = \mathbf{U}\boldsymbol{\Sigma}\mathbf{V}^{\mathrm{T}}$) when the local method is adopted, as discussed in [45], for example. Then, for this reduction, one discards left singular vectors whose singular values do not satisfy $\sigma_j / \max(\mathrm{diag}(\boldsymbol{\Sigma})) > \epsilon$, where σ_j denotes the j^{th} singular value (j^{th} entry on the diagonal of $\boldsymbol{\Sigma}$), and ϵ represents an additional parameter (threshold) that must be introduced. It plays a similar role to the $\mathrm{TV}_{\mathrm{MAC}}$ used in the proposed (global) approach; both thresholds are effectively employed to rank-reduce $\boldsymbol{\Psi}_{\mathrm{LR}}$. As proposed by several researchers,

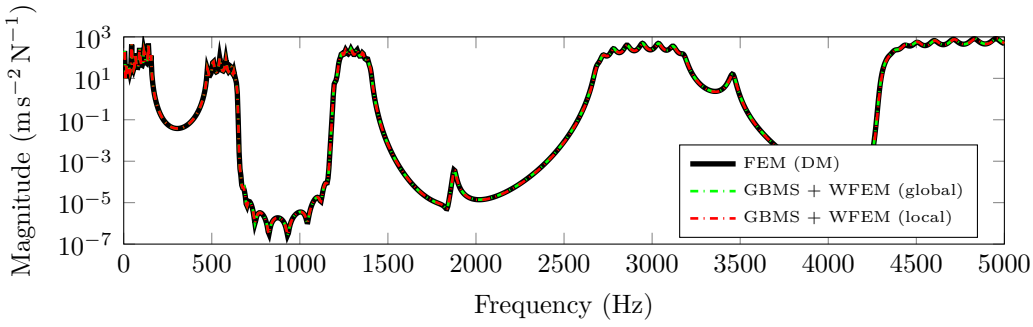

(a)

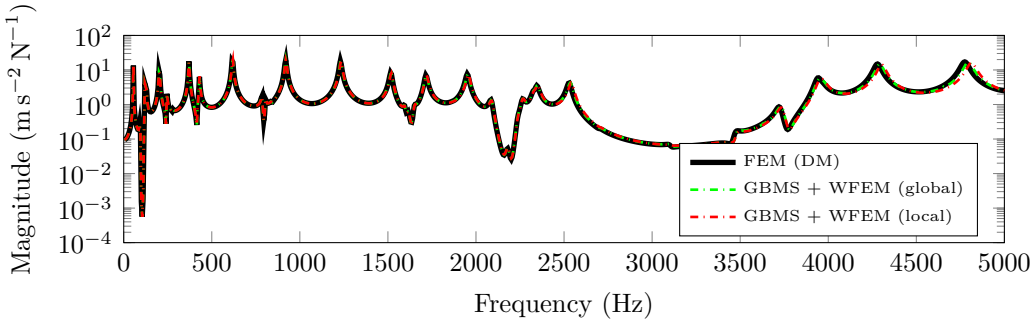

(b)

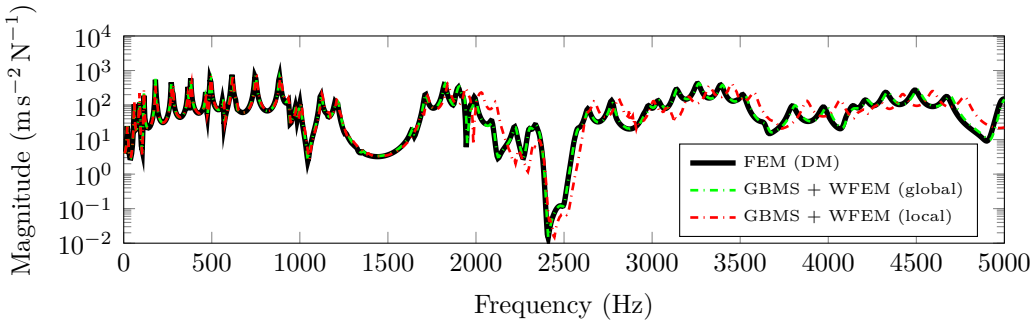

(c)

Figure 15: Comparison between the magnitudes of accelerance-type FRFs calculated for (a) the PC incorporating IAM; (b) the EM with rectangular spiral resonators; and (c) the PC with an internal void of arbitrary shape. These FRFs were obtained by the traditional FEM employing the DM and the WFEM with boundary and internal DoFs of the unit cell reduced. For the WFEM, both global ($\hat{n} = 5$, $\bar{n} = 1.2$, and $\mathrm{TV_{MAC}} = 0.6$) and local ($\hat{n} = 5$, $\bar{n} = 1.2$, and $\epsilon = 1 \times 10^{-4}$) approaches were adopted. The corresponding input and output DoFs used to calculate these FRFs are shown in Figs. 3c, 8c, and 10c.

e.g., [45, 64, 88, 89], the threshold value $\epsilon = 1 \times 10^{-4}$ is used in the following.

The results given in Fig. 15 indicate that, in general, the global (unit cell-level) reduction process which is reported in this work seems to provide more accurate FRFs than the local approach. Although Fig. 15a does not reveal noticeable differences between the FRFs calculated for the IAM-based PC using the global and local approaches, Figs. 15b and 15c show increasing errors when using the local approach, particularly for the PC with internal void. Table 4 presents the relative error norm [90] between the reference curves and those obtained with the WFEM, considering the reduction of boundary DoFs using both the local and global approaches, over the whole analyzed frequency range. As clearly observed, the proposed (global) reduction method consistently yields lower error norms in comparison with the local approach.

Table 4: Relative error norm between the reference curves and those obtained with the WFEM in Fig. 15, considering the reduction of boundary DoFs using both the local and global approaches. For both cases, the reduction of internal DoFs is performed with the CB method.

Method used for reducing the boundary DoFs	PC incorporating IAM (Fig. 15a)	EM with rectangular spiral resonators (Fig. 15b)	PC with an internal void of arbitrary shape (Fig. 15c)
Local	0.06	0.34	0.62
Global (proposed)	0.03	0.20	0.18

Possible sources for the discrepancies between the FRFs presented in Fig. 15, obtained by reducing the boundary DoFs globally, as proposed, or locally, should also be of interest. Note that, for both cases, the boundary DoFs are reduced following similar procedures, differing solely on the construction of $\mathbf{\Psi}_{\mathrm{LR}}$. First, the FRFs in Figs. 15a and 15b, calculated using the local approach, are less accurate than those obtained with the global approach (cf. Table 4), which seems due to insufficient numbers of modal DoFs being employed to reduce the boundary DoFs of the unit cells, as summarized in Table 5. In this table, the numbers of modal, boundary DoFs related with the unit cells containing IAM and local resonators in the shape of rectangular spirals are lower when the local approach is used, in comparison with those resulting for the global method. On the other hand, the significant discrepancies between the FRFs obtained using the local and global reduction of boundary DoFs in Fig. 15c do not bear the same cause, as Table 5 reveals that more modal DoFs are employed by the local approach. This suggests that the eigenvectors calculated using Eq. (14) can provide a more effective basis for reducing the boundary DoFs than those obtained from Eq. (46).

This can possibly be explained by the fact that the eigenvectors calculated from Eq. (14) take into account the dynamic behavior of the whole unit cell, which appears to significantly influence the accuracy of the model reduction process. In fact, the third example investigated in this work, shown in Fig. 10c, is characterized by a unit cell whose interfaces' dynamic behavior cannot be well described "in isolation", by means of eigenvectors retrieved from a local eigenproblem, over the entire analyzed frequency range, an observation which is conjectured to have its roots on the particular geometric features of the unit cell (which ultimately determine its overall dynamics).

Table 5: Unit cell model-size details with boundary DoFs reduced using the global approach (cf. Tables 1, 2, and 3) and the local approach. For the global method, $\hat{n} = 5$, $\bar{n} = 1.2$, and $\mathrm{TV}_{\mathrm{MAC}} = 0.6$ were used, while for the local method, $\hat{n} = 5$, $\bar{n} = 1.2$, and $\epsilon = 1 \times 10^{-4}$ were applied. In all examples, the number of internal DoFs remains unchanged regardless of whether the local or global approach is used, as $\hat{n} = 5$ for both cases.

Set of equations	PC incorporating IAM (Fig. 3b)		EM with rectangular spiral resonators (Fig. 8b)		PC with an internal void of arbitrary shape (Fig. 10b)	
	Global (Table 1)	Local	Global (Table 2)	Local	Global (Table 3)	Local
Boundary	32	6	112	48	86	100
Internal	38	38	60	60	54	54
Complete	70	44	172	108	140	154

4.4.2. Comparing MAC- and SVD-based procedures for reduction of boundary modes

Although the previous results indicate that the reduction of boundary DoFs using the proposed (global) approach performs better than the local method, one further investigates both model reduction techniques by varying the number of boundary DoFs and considering that they can be truncated using the MAC or SVD procedures. Accordingly, Fig. 16 presents the relative error norm between reference and WFEM-related FRFs and the corresponding number of boundary DoFs related to the calculation of FRFs for the PC with an internal void of arbitrary shape, assuming the input and output locations depicted in Fig. 10c. In both cases, the reduction of boundary DoFs is performed using the same parameters introduced previously, i.e., $\hat{n} = 5$ and $\mathrm{TV}_{\mathrm{MAC}} = 0.6$ for the global approach, and $\hat{n} = 5$ and $\epsilon = 1 \times 10^{-4}$ for the local strategy. The value of $\bar{n}$ is varied as a free parameter, so one is able to assess its influence on the quantities of interest. Note that the number of internal DoFs (fixed interface modes in the CB MOR) equals 54 for all cases, as $\hat{n} = 5$.

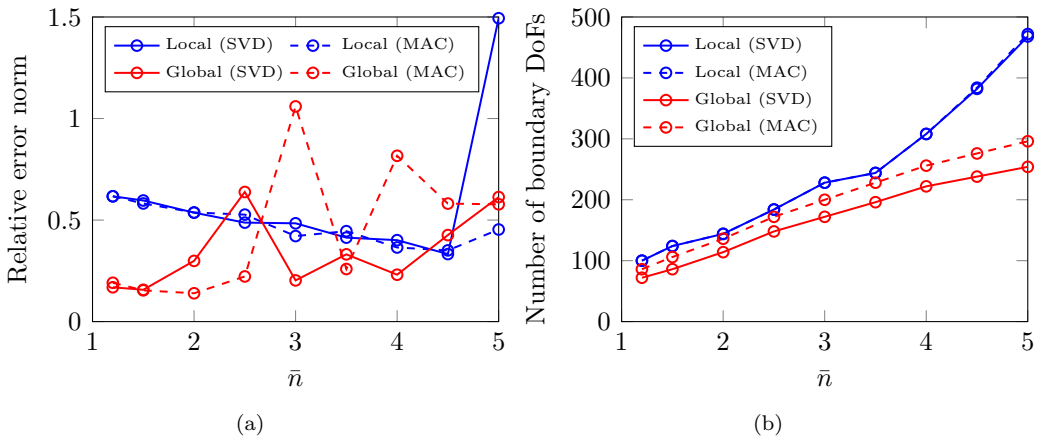

Figure 16: Relative error norm between reference and WFEM-related FRFs (a) and the corresponding number of boundary DoFs (b), calculated for the PC with an internal void of arbitrary shape. In the WFEM, the reduction of boundary DoFs is performed using either the local or global approach, with the parameters $\hat{n} = 5$ and $\mathrm{TV}_{\mathrm{MAC}} = 0.6$ used for the global approach, and $\hat{n} = 5$ and $\epsilon = 1 \times 10^{-4}$ for the local strategy. The number of internal DoFs equals 54 for all cases, as $\hat{n} = 5$.

Firstly, Fig. 16a reveals that the FRFs calculated by reducing the boundary DoFs using eigenvectors computed from Eq. (14) (global approach) are, in general, much more accurate than those obtained using eigenvectors derived from Eq. (46) (local approach), further highlighting what has been discussed previously and shown in Fig. 15 and Table 4. In fact, the minimum relative error attained by computing FRFs using the local approach, employing either the SVD or MAC-based procedures for filtering modal, boundary DoFs, considering $\hat{n} = 5$ and $\epsilon = 1 \times 10^{-4}$, is 0.33 for $\bar{n} = 4.5$ (cf. the solid blue curve), which is more than twice as large as the relative error norm achieved with the global approach for $\bar{n} = 1.2$, equal to 0.16, with $\hat{n} = 5$, $\mathrm{TV}_{\mathrm{MAC}} = 0.6$ (cf. the solid red curve). Overall, the curves plotted in Fig. 16a show that larger values of $\bar{n}$ can deteriorate the accuracy of harmonic forced responses, due to challenges in the computation of high-order evanescent wave modes (cf. discussions in Subsection 4.1) for both local and global reduction strategies. Interestingly, the MAC-based mode selection procedure can make the computation of harmonic forced responses by the WFEM more stable compared to the SVD technique, for lower $\bar{n}$ values, when the reduction of boundary DoFs is performed using the proposed (global) approach (cf. the dashed red curve). On the other hand, both the MAC and SVD-based

frequency truncation techniques play a similar role, removing some redundant boundary modes when the local eigenvalue problem given by Eq. (46) is solved, considering $\bar{n}$ ranging from 1.2 to 4.5 (solid and dashed blue curves). For $\bar{n} = 5$, the same curves show that the MAC can be advantageous over the SVD technique, as it allows the computation of a FRF with lower relative error norm between the reference and WFEM-related results.

To complement the results presented in Fig. 16a, Fig. 16b shows that the number of boundary DoFs monotonically increases as $\bar{n}$ grows. Particularly, the truncation techniques based on the MAC and SVD seem to have negligible influence on the number of boundary DoFs when the local eigenproblem is used to obtain the interface modes in the L-CC model-order reduction scheme. This result is consistent with previous discussions regarding the relative error norm for the corresponding curves in Fig. 16a. In contrast, when the global approach is employed, the SVD penalizes the number of boundary DoFs more heavily than the MAC (red curves in Fig. 16b). One should also emphasize that the increasing number of boundary DoFs seen in Fig. 16b, as $\bar{n}$ grows, is problematic for the wave-based approach because it significantly increases computational cost and may introduce numerical instabilities in the computation of FRFs and other responses — recall that the sizes of wave-based matrices reviewed in Subsection 3.1 are directly related to the number of boundary DoFs.

The results displayed in Fig. 16b additionally reveal that the number of boundary DoFs associated with the minimum relative error of 0.33 in Fig. 16a, achieved for $\bar{n} = 4.5$ when computing FRFs using the local approach with the SVD-based truncation technique corresponds to 382. On the other hand, the relative error of 0.16, achieved when the global approach is used adopting $\bar{n} = 1.2$, is related with only 72 boundary DoFs, which is significantly lower than the number obtained with the local approach.

These remarks add further support to the claim one has already discussed, that eigenvectors obtained from Eq. (14) (global approach) can improve the model reduction process in comparison to the traditional strategy currently reported in the literature [31, 34, 35, 40–43, 45], which relies on eigenvectors from Eq. (46) to reduce boundary DoFs. Besides, Figs. 16a and 16b likewise show that the reduction of boundary DoFs using the local approach exhibits a very slow convergence of the relative error norm for the response of interest, as $\bar{n}$ increases. This means that, for unit cell model reduction using the L-CC method with eigenvectors from a local eigenproblem, increasing the number of boundary DoFs yields only marginal improvements to the relative error

norm, even when the referred increase is substantial.

Other aspects should be clarified, which make us believe MAC indices can be more advantageous for selecting the most relevant boundary DoFs than the SVD-based approach. Firstly, recall that the singular value decomposition of $\boldsymbol{\Psi}_{\mathrm{LR}} = \mathbf{U}\boldsymbol{\Sigma}\mathbf{V}^{\mathrm{T}}$, whether $\boldsymbol{\psi}_{\mathrm{L}}$ and $\boldsymbol{\psi}_{\mathrm{R}}$ are determined from Eq. (14) or (46). To rank-reduce $\boldsymbol{\Psi}_{\mathrm{LR}}$ directly through its SVD, it is replaced by $\mathbf{U}$ ($\boldsymbol{\Psi}_{\mathrm{LR}} \rightarrow \mathbf{U}$), taking into account those left singular vectors in $\mathbf{U}$ related to the largest

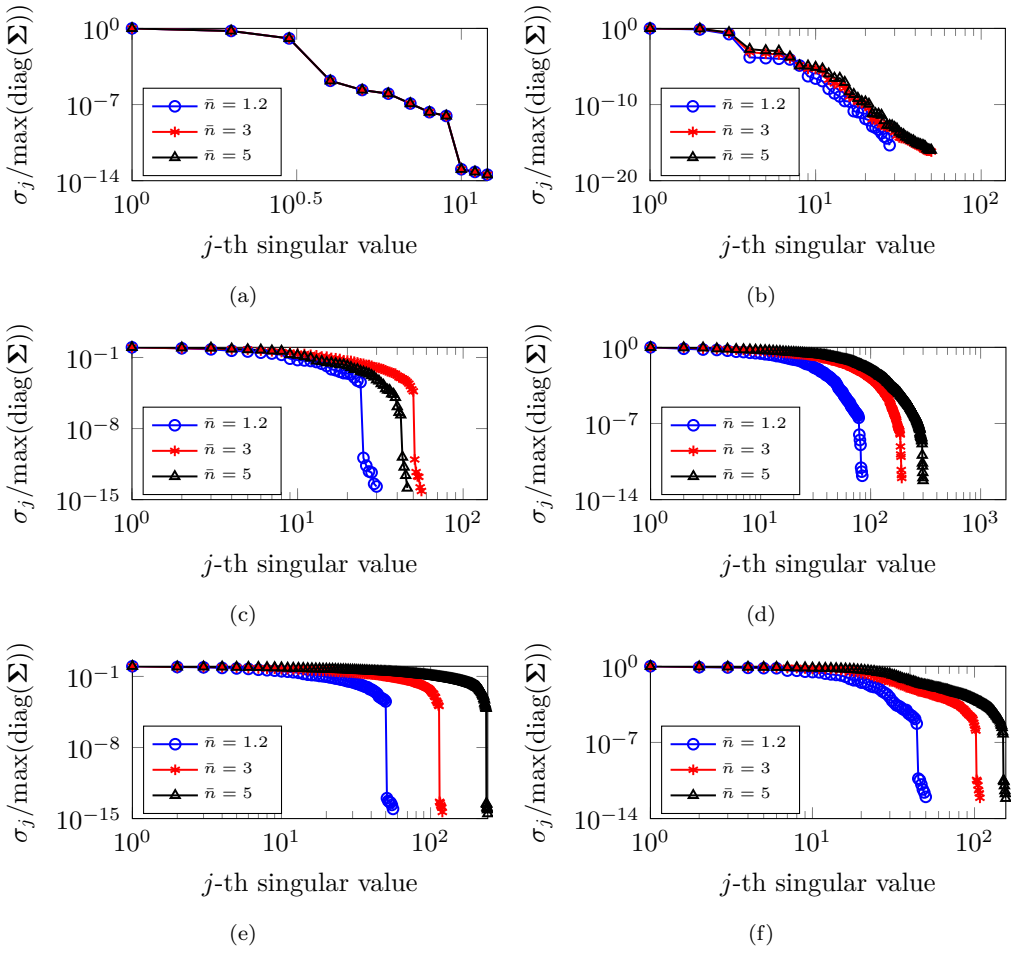

Figure 17: Normalized singular values ($\sigma_j/\max(\mathrm{diag}(\boldsymbol{\Sigma}))$) calculated for the PC incorporating IAM (a–b), EM with rectangular spiral resonators (c–d), and PC with an internal void of arbitrary shape (e–f), considering that the reduction of boundary DoFs is performed using the local (left) or global (right) approaches, for $\hat{n} = 5$.

singular values, based on the criterion $\sigma_j/\max(\mathrm{diag}(\boldsymbol{\Sigma})) > \epsilon$, for example [45]. It turns out that, even for the same unit cell, the singular values σ_j, which are used as a metric during the truncation of left singular modes, can be altered due to changes in the input basis $\boldsymbol{\Psi}_{\mathrm{LR}}$ that arise as $\bar{n}$ is varied, for instance. This issue is illustrated in Fig. 17, where $\sigma_j/\max(\mathrm{diag}(\boldsymbol{\Sigma}))$ is plotted for all unit cells investigated in this work, considering $\bar{n}$ equal to 1.2, 3, and 5, as well as $\boldsymbol{\psi}_{\mathrm{L}}$ and $\boldsymbol{\psi}_{\mathrm{R}}$ computed using the local (Eq. (46)) and global (Eq. (14)) eigenproblems. These changes in the singular values can influence the reduction of boundary DoFs, as they alter the number of equations retained in the resulting modal basis, which is then used as a projection operator in the L-CC method (matrix $\boldsymbol{\Psi}_{\mathrm{LR}}$), and should, thus, be a point of attention. Another issue that can appear when the SVD approach is employed to truncate boundary DoFs is that, depending on the unit cell, the magnitudes of sequential singular values (j and $j+1$, for example) can involve an abrupt jump, which potentially makes challenging for one to define or choose a consistent truncation threshold ϵ (cf. Fig. 17, for example). Such abrupt changes may cause the exclusion of important modes during the SVD-based truncation process, which is particularly concerning when they are related to the first singular values, having the potential to compromise the quality of reduced-order models depending on the value of ϵ.

The MAC-based truncation criterion introduced in Section 2.3 and discussed through this work, in turn, does not face the previously discussed issues, as it focuses on the degree of similarity between the shapes of modes at the left and right interfaces of a unit cell by calculating their MAC indices, which serves as a truncation metric. Accordingly, the MAC is not as sensitive to the input basis being influenced by $\bar{n}$, for example, as the SVD is; and it is not susceptible to abrupt changes in MAC indices, as typically occur for singular values in the SVD approach, due to their dependence on the algebraic structure of this decomposition. Therefore, in one's assessment, the MAC indices can be explored in a mathematically robust criterion, ensuring a more stable, physically meaningful, and consistent selection of boundary DoFs for reducing the model of a given unit cell.

5. Concluding remarks

This work has focused on computing harmonic forced responses of periodic structures using the WFEM combined with a modified GBMS, employing size-reduced unit cell FE models. Firstly, the internal DoFs of the unit

cell models were reduced using the CB model reduction method, utilizing fixed-interface modes and constraint modes. Then, the remaining boundary DoFs, which correspond to physical coordinates, were reduced using L-CC, where the following improvements have been considered:

1. An eigenvalue problem at the global level of the unit cell was solved after applying the CB method to determine the boundary modes, in contrast to a local eigenproblem, as currently considered in the literature;
2. A MAC-based mode selection procedure was employed to remove redundant modes from the L-CC transformation matrix, while respecting constraints imposed by the periodicity conditions of the Bloch-Floquet theorem. This task has been alternatively performed using SVD in the literature.

Numerical simulations demonstrated that highly-reduced unit cell FE models can be obtained using the CB and L-CC model reduction methods.

By leveraging the advantages of the WFEM, harmonic forced responses for three types of unit cells (an IAM-based PC, an EM with rectangular spiral resonators, and a PC with an internal void of arbitrary shape and several boundary DoFs) were rapidly and accurately computed, showing minimal deviations compared to reference solutions. In the worst case, the relative error between resonance frequencies of the models was smaller than 1.2%, partially attributed to the frequency discretization adopted for computations. In terms of FRFs amplitudes, CSF values mostly did not fall below 0.9, indicating minimal discrepancies between the responses obtained using the FEM and those obtained using the WFEM with the proposed model reduction strategy. In all cases, numerical simulations demonstrated that the proposed improvements in the reduction of boundary DoFs are of utmost importance to ensure high accuracy of the reduced models, especially for unit cells incorporating geometric features that render their boundary motions largely influenced by their interior DoFs. Specifically, since an eigenvalue problem is solved at the global level of the unit cell, it has been found that frequency-based truncation criterion can be effectively used to determine modal bases for the L-CC, as opposed to the local strategy available in literature. In addition, simulations have also illustrated the robustness of the MAC-based truncation procedure against the method based on SVD.

Lastly, it has been demonstrated that reduced-order unit cell models can mitigate numerical issues that often occur when computing harmonic forced responses using the WFEM by avoiding the calculation of computationally-

troublesome highly-evanescent wave modes. Therefore, this work extends the WFEM to challenging structural dynamics problems, involving unit cell models with several DoFs and analyses in the mid- to high-frequency bands.

Future work perspectives include implementing algebraic condensation to reduce both interior and boundary DoFs, aiming to further accelerate the analysis of periodic structures using the WFEM and GBMS, and accounting for the effect of residual modes during their reduction. Another relevant topic consists of assessing the influence of other types of loads, such as distributed ones, and of where they are applied, over the performance and accuracy of the proposed modifications to the GBMS strategy for computation of harmonic forced responses of periodic structures.

Acknowledgements

This study was financed, in part, by the São Paulo Research Foundation (FAPESP), Brasil. Process Numbers #2018/15894-0, #2023/11207-7 and #2024/07549-2. All authors are grateful to FAPESP for the provided grants. V. M. S. Santos also acknowledges the Brazilian Coordination for the Improvement of Higher Education Personnel (CAPES). M. Ouisse acknowledges the graduate school EIPHI (project ANR-17-EURE-0002).

References

[1] M. I. Hussein, M. J. Leamy, M. Ruzzene, Dynamics of Phononic Materials and Structures: Historical Origins, Recent Progress, and Future Outlook, Appl. Mech. Rev. 66 (2014). doi:10.1115/1.4026911.

[2] Y.-F. Wang, Y.-Z. Wang, B. Wu, W. Chen, Y.-S. Wang, Tunable and Active Phononic Crystals and Metamaterials, Appl. Mech. Rev. 72 (2020). doi:10.1115/1.4046222.

[3] N. Gao, Z. Zhang, J. Deng, X. Guo, B. Cheng, H. Hou, Acoustic Metamaterials for Noise Reduction: A Review, Adv. Mater. Technol. 7 (2022). doi:10.1002/admt.202100698.

[4] T.-T. Wang, Y.-F. Wang, Z.-C. Deng, V. Laude, Y.-S. Wang, Reconfigurable waveguides defined by selective fluid filling in two-dimensional phononic metaplates, Mech. Syst. Signal Pr. 165 (2022) 108392. doi:10.1016/j.ymssp.2021.108392.

[5] L. Ning, Y.-Z. Wang, Y.-S. Wang, Active control cloak of the elastic wave metamaterial, Int. J. Solids Struct. 202 (2020) 126–135. doi:10.1016/j.ijsolstr.2020.06.009.

[6] G. Lee, J. Park, W. Choi, B. Ji, M. Kim, J. Rho, Multiband elastic wave energy localization for highly amplified piezoelectric energy harvesting using trampoline metamaterials, Mech. Syst. Signal Pr. 200 (2023) 110593. doi:10.1016/j.ymssp.2023.110593.

[7] M. Badreddine Assouar, M. Senesi, M. Oudich, M. Ruzzene, Z. Hou, Broadband plate-type acoustic metamaterial for low-frequency sound attenuation, Appl. Phys. Lett. 101 (2012). doi:10.1063/1.4764072.

[8] Z. Jia, Z. Sun, Q. Tian, Y. Luo, X. Zhang, S. Zhao, Z. Kang, Optimization design of all-angle negative refraction phononic crystals at a specified frequency, Mech. Syst. Signal Pr. 205 (2023) 110824. doi:10.1016/j.ymssp.2023.110824.

[9] K. Yi, M. Ouisse, E. Sadoulet-Reboul, G. Matten, Active metamaterials with broadband controllable stiffness for tunable band gaps and non-reciprocal wave propagation, Smar. Mat. St. 28 (2019) 065025. doi:10.1088/1361-665x/ab19dc.

[10] H. Wang, Y. Xu, P. Genevet, J.-H. Jiang, H. Chen, Broadband mode conversion via gradient index metamaterials, Sci. Rep. 6 (2016). doi:10.1038/srep24529.

[11] Y. Chen, Z. Shao, J. Wei, J. Feng, P. Sareh, Geometric design and performance analysis of a foldcore sandwich acoustic metastructure for tunable low-frequency sound absorption, Finite Elem. Anal. Des. 235 (2024) 104150. doi:10.1016/j.finel.2024.104150.

[12] M. A. Attarzadeh, M. Nouh, Non-reciprocal elastic wave propagation in 2D phononic membranes with spatiotemporally varying material properties, J. Sound Vib. 422 (2018) 264–277. doi:10.1016/j.jsv.2018.02.028.

[13] V. F. Almeida, V. D. Lima, J. R. F. Arruda, Applying the phononic crystal concept to the intake muffler of a refrigeration compressor, Appl. Acoust. 194 (2022) 108800. doi:10.1016/j.apacoust.2022.108800.

[14] Q. Wang, J. Li, Y. Zhang, Y. Xue, F. Li, Bandgap properties in metamaterial sandwich plate with periodically embedded plate-type resonators, Mech. Syst. Signal Pr. 151 (2021) 107375. doi:10.1016/j.ymssp.2020.107375.

[15] Z. Wu, W. Liu, F. Li, C. Zhang, Band-gap property of a novel elastic metamaterial beam with X-shaped local resonators, Mech. Syst. Signal Pr. 134 (2019) 106357. doi:10.1016/j.ymssp.2019.106357.

[16] E. J. P. Miranda, E. D. Nobrega, A. H. R. Ferreira, J. M. C. Dos Santos, Flexural wave band gaps in a multi-resonator elastic metamaterial plate using Kirchhoff-Love theory, Mech. Syst. Signal Pr. 116 (2019) 480–504. doi:10.1016/j.ymssp.2018.06.059.

[17] Y. Xiao, J. Wen, G. Wang, X. Wen, Theoretical and Experimental Study of Locally Resonant and Bragg Band Gaps in Flexural Beams Carrying Periodic Arrays of Beam-Like Resonators, J. Vib. Acoust. 135 (2013). doi:10.1115/1.4024214.

[18] Q. Zhang, K. Zhang, G. Hu, Tunable fluid-solid metamaterials for manipulation of elastic wave propagation in broad frequency range, Appl. Phys. Lett. 112 (2018). doi:10.1063/1.5023307.

[19] L. S. Prado, T. G. Ritto, Vibration reduction of a rotating machine using resonator rings, Mech. Res. Commun. 107 (2020) 103533. doi:10.1016/j.mechrescom.2020.103533.

[20] T.-T. Wang, Y.-F. Wang, Z.-C. Deng, V. Laude, Y.-S. Wang, Reconfigurable coupled-resonator acoustoelastic waveguides in fluid-filled phononic metaplates, Compos. Struct. 303 (2023) 116355. doi:10.1016/j.compstruct.2022.116355.

[21] L. Xiao, O. S. Bursi, M. Wang, S. Nagarajaiah, F. Sun, X.-L. Du, Metamaterial beams with negative stiffness absorbers and rotation: band-gap behavior and band-gap merging, Eng. Struct. 280 (2023) 115702. doi:10.1016/j.engstruct.2023.115702.

[22] S. Ahsani, R. Boukadia, C. Droz, C. Claeys, E. Deckers, W. Desmet, Diffusion based homogenization method for 1D wave propagation, Mech. Syst. Signal Pr. 136 (2020) 106515. doi:10.1016/j.ymssp.2019.106515.

[23] C. Yang, K. Kaynardag, S. Salamone, Investigation of wave propagation and attenuation in periodic supported rails using wave finite element method, Acta Mech. (2023). doi:10.1007/s00707-023-03484-8.

[24] E. J. P. d. Miranda Jr., J. M. C. D. Santos, Flexural Wave Band Gaps in Phononic Crystal Euler-Bernoulli Beams Using Wave Finite Element and Plane Wave Expansion Methods, Mater. Res. 20 (2018) 729–742. doi:10.1590/1980-5373-mr-2016-0877.

[25] V. F. D. Poggetto, A. L. Serpa, Elastic wave band gaps in a three-dimensional periodic metamaterial using the plane wave expansion method, Int. J. Mech. Sci. 184 (2020) 105841. doi:10.1016/j.ijmecsci.2020.105841.

[26] V. Romero-García, J. V. Sánchez-Pérez, L. M. Garcia-Raffi, Propagating and evanescent properties of double-point defects in sonic crystals, New J. Phys. 12 (2010) 083024. doi:10.1088/1367-2630/12/8/083024.

[27] L. F. C. Schalcher, J. M. C. D. Santos, E. J. P. Miranda, Extended plane wave expansion formulation for 1-D viscoelastic phononic crystals, Partial Differ. Equ. Appl. 7 (2023) 100489. doi:10.1016/j.padiff.2023.100489.

[28] U. Lee, Spectral Element Method in Structural Dynamics, Wiley, 2009. doi:10.1002/9780470823767.

[29] J. F. Doyle, Wave Propagation in Structures, Springer International Publishing, 2021. doi:10.1007/978-3-030-59679-8.

[30] D. Krattiger, M. I. Hussein, Bloch mode synthesis: Ultrafast methodology for elastic band-structure calculations, Phys. Rev. E 90 (2014) 063306. doi:10.1103/physreve.90.063306.

[31] D. Krattiger, M. I. Hussein, Generalized Bloch mode synthesis for accelerated calculation of elastic band structures, J. Comput. Phys. 357 (2018) 183–205. doi:10.1016/j.jcp.2017.12.016.

[32] B. G. Christoff, H. Brito-Santana, R. Talreja, V. Tita, Development of an ABAQUS™ plug-in to evaluate the fourth-order elasticity tensor of a periodic material via homogenization by the asymptotic expansion

method, Finite Elem. Anal. Des. 181 (2020) 103482. doi:10.1016/j.finel.2020.103482.

[33] J.-M. Mencik, On the low- and mid-frequency forced response of elastic structures using wave finite elements with one-dimensional propagation, Comput. Struct. 88 (2010) 674–689. doi:10.1016/j.compstruc.2010.02.006.

[34] C. Xi, H. Zheng, Improving the generalized Bloch mode synthesis method using algebraic condensation, Comput. Method. Appl. M. 379 (2021) 113758. doi:10.1016/j.cma.2021.113758.

[35] X. Zhu, C. Xi, H. Zheng, An improvement of generalized Bloch mode synthesis method-based model order reduction technique for band-structure computation of periodic structures, Comput. Struct. 281 (2023) 107013. doi:10.1016/j.compstruc.2023.107013.

[36] W. C. Hurty, Vibrations of Structural Systems by Component Mode Synthesis, J. Eng. Mech. Div. 86 (1960) 51–69. doi:10.1061/jmcea3.0000162.

[37] R. R. Craig, M. C. C. Bampton, Coupling of substructures for dynamic analyses., AIAA J. 6 (1968) 1313–1319. doi:10.2514/3.4741.

[38] A. Aladwani, A refined Bloch mode synthesis framework for fast and accurate analysis of electroelastic metamaterials with piezoelectric resonant shunt damping, Mech. Syst. Signal Pr. 180 (2022) 109380. doi:10.1016/j.ymssp.2022.109380.

[39] A. Aladwani, M. Nouh, M. I. Hussein, State-space Bloch mode synthesis for fast band-structure calculations of non-classically damped phononic materials, Comput. Method. Appl. M. 396 (2022) 115018. doi:10.1016/j.cma.2022.115018.

[40] L. Van Belle, N. G. R. M. Filho, M. C. Villanueva, C. Claeys, E. Deckers, F. Naets, W. Desmet, Fast metamaterial design optimization using reduced order unit cell modeling, in: Proc. of ISMA 2020, 2020, pp. 2487–2502.

[41] V. Cool, F. Naets, L. Van Belle, W. Desmet, E. Deckers, Accelerated dispersion curve calculations for periodic vibro-acoustic structures, Front. Mech. Eng. 8 (2022). doi:10.3389/fmech.2022.995322.

[42] V. Cool, L. Van Belle, C. Claeys, E. Deckers, W. Desmet, Impact of the Unit Cell Choice on the Efficiency of Dispersion Curve Calculations Using Generalized Bloch Mode Synthesis, J. Vib. Acoust. 144 (2021). doi:10.1115/1.4051817.

[43] L. Van Belle, C. Claeys, E. Deckers, W. Desmet, Fast forced response calculations of finite metamaterial plates using a Generalized Bloch Mode Synthesis based sub-structuring approach, in: Proc. of Euronoise, Sociedade Portuguesa de Acústica (SPA), 2021, pp. 1323–1332.

[44] D. Jiang, S. Zhang, Y. Li, B. Chen, N. Li, A hybrid Bloch mode synthesis method based on the free interface component mode synthesis method, J. Comput. Phys. 496 (2024) 112556. doi:10.1016/j.jcp.2023.112556.

[45] D. Duhamel, J.-M. Mencik, Reduced-order modeling for time domain analysis of finite periodic structures with absorbing boundary conditions, J. Sound Vib. 590 (2024) 118576. doi:10.1016/j.jsv.2024.118576.

[46] M. I. Hussein, Reduced Bloch mode expansion for periodic media band structure calculations, Proc. Math. Phys. Eng. Sci. 465 (2009) 2825–2848. doi:10.1098/rspa.2008.0471.

[47] R. F. Boukadia, C. Droz, M. N. Ichchou, W. Desmet, A Bloch wave reduction scheme for ultrafast band diagram and dynamic response computation in periodic structures, Finite Elem. Anal. Des. 148 (2018) 1–12. doi:10.1016/j.finel.2018.05.007.

[48] C. Droz, R. Boukadia, W. Desmet, A multi-scale model order reduction scheme for transient modelling of periodic structures, J. Sound Vib. 510 (2021) 116312. doi:10.1016/j.jsv.2021.116312.

[49] W. Wang, A. V. Amirkhizi, Reduced Order Modeling of Dynamic Mechanical Metamaterials for Analysis of Infinite and Finite Systems, J. Appl. Mech. 90 (2023). doi:10.1115/1.4062888.

[50] M. N. Ichchou, J.-M. Mencik, W. Zhou, Wave finite elements for low and mid-frequency description of coupled structures with damage, Comput.

Method. Appl. M. 198 (2009) 1311–1326. doi:10.1016/j.cma.2008.11.024.

[51] J.-M. Mencik, D. Duhamel, A wave finite element-based approach for the modeling of periodic structures with local perturbations, Finite Elem. Anal. Des. 121 (2016) 40–51. doi:10.1016/j.finel.2016.07.010.

[52] D. S. Claro, V. Denis, J.-M. Mencik, Defect localization in waveguide assemblies with curved joints via wave finite elements and time of flight analysis, Eur. J. Mech. A. Solids 97 (2023) 104814. doi:10.1016/j.euromechsol.2022.104814.

[53] B. R. Mace, E. Manconi, Modelling wave propagation in two-dimensional structures using finite element analysis, J. Sound Vib. 318 (2008) 884–902. doi:10.1016/j.jsv.2008.04.039.

[54] C. W. Zhou, J. P. Lainé, M. N. Ichchou, A. M. Zine, Multi-scale modelling for two-dimensional periodic structures using a combined mode/wave based approach, Comput. Struct. 154 (2015) 145–162. doi:10.1016/j.compstruc.2015.03.006.

[55] A. Palermo, A. Marzani, Extended bloch mode synthesis: Ultrafast method for the computation of complex band structures in phononic media, Int. J. Solids Struct. 100–101 (2016) 29–40. doi:10.1016/j.ijsolstr.2016.06.033.

[56] Y. Yang, B. R. Mace, M. J. Kingan, Vibroacoustic analysis of periodic structures using a wave and finite element method, J. Sound Vib. 457 (2019) 333–353. doi:10.1016/j.jsv.2019.06.009.

[57] D. Duhamel, Computation of the dynamic scalar response of large two-dimensional periodic and symmetric structures by the wave finite element method, Finite Elem. Anal. Des. 230 (2024) 104096. doi:10.1016/j.finel.2023.104096.

[58] J.-M. Mencik, A wave finite element approach for the analysis of periodic structures with cyclic symmetry in dynamic substructuring, J. Sound Vib. 431 (2018) 441–457. doi:10.1016/j.jsv.2018.05.027.

[59] J.-G. Kim, K.-H. Lee, P.-S. Lee, Estimating relative eigenvalue errors in the Craig-Bampton method, Comput. Struct. 139 (2014) 54–64. doi:10.1016/j.compstruc.2014.04.008.

[60] R. J. Guyan, Reduction of stiffness and mass matrices, AIAA J. 3 (1965) 380–380. doi:10.2514/3.2874.

[61] MATLAB, version 9.14.0 (R2023a), The MathWorks Inc., 2023.

[62] N. M. M. Maia, J. M. M. e Silva, J. He, N. A. J. Lieven, R. M. Lin, G. W. Skingle, W.-M. To, A. P. V. Urgueira, Theoretical and Experimental Modal Analysis, Research Studies Press LTD., 1997.

[63] D. J. Ewins, Modal Testing: Theory, Practice and Application, Wiley, 2009.

[64] D. Krattiger, L. Wu, M. Zacharczuk, M. Buck, R. J. Kuether, M. S. Allen, P. Tiso, M. R. W. Brake, Interface reduction for Hurty/Craig-Bampton substructured models: Review and improvements, Mech. Syst. Signal Pr. 114 (2019) 579–603. doi:10.1016/j.ymssp.2018.05.031.

[65] J.-M. Mencik, D. Duhamel, A wave-based model reduction technique for the description of the dynamic behavior of periodic structures involving arbitrary-shaped substructures and large-sized finite element models, Finite Elem. Anal. Des. 101 (2015) 1–14. doi:10.1016/j.finel.2015.03.003.

[66] T. Hoang, D. Duhamel, G. Foret, Wave finite element method for waveguides and periodic structures subjected to arbitrary loads, Finite Elem. Anal. Des. 179 (2020) 103437. doi:10.1016/j.finel.2020.103437.

[67] J. M. Renno, B. R. Mace, On the forced response of waveguides using the wave and finite element method, J. Sound Vib. 329 (2010) 5474–5488. doi:10.1016/j.jsv.2010.07.009.

[68] V. M. S. Santos, Numerical Investigation of Wave Propagation in Beams Coupled to Metastructures Combining Spectral and Wave-Finite Element Methods, Master's thesis, Aeronautics Institute of Technology, 2022.

[69] B. R. Mace, D. Duhamel, M. J. Brennan, L. Hinke, Finite element prediction of wave motion in structural waveguides, J. Acoust. Soc. Am. 117 (2005) 2835–2843. doi:10.1121/1.1887126.

[70] R. G. Salsa Junior, T. d. P. Sales, D. A. Rade, Optimization of Vibration Band Gaps in Damped Lattice Metamaterials, Lat. Am. J. Solids Stru. 20 (2023). doi:10.1590/1679-78257486.

[71] J.-M. Mencik, New advances in the forced response computation of periodic structures using the wave finite element (WFE) method, Comput. Mech. 54 (2014) 789–801. doi:10.1007/s00466-014-1033-1.

[72] Y. Waki, B. R. Mace, M. J. Brennan, Numerical issues concerning the wave and finite element method for free and forced vibrations of waveguides, J. Sound Vib. 327 (2009) 92–108. doi:10.1016/j.jsv.2009.06.005.

[73] P. B. Silva, Dynamic analysis of periodic structures via wave-based numerical approaches and substructuring techniques, Ph.D. thesis, Campinas State University, 2015.

[74] Y. Waki, B. R. Mace, M. J. Brennan, On Numerical Issues for the Wave/Finite Element Method, Technical Memorandum No. 964, University of Southampton, Institute of Sound & Vibration Research, 2006.

[75] J. Angeles, S. Bai, Kinematics of Mechanical Systems: Fundamentals, Analysis and Synthesis, Springer International Publishing, 2022. doi:10.1007/978-3-031-09544-3.

[76] D. Duhamel, B. R. Mace, M. J. Brennan, Finite element analysis of the vibrations of waveguides and periodic structures, J. Sound Vib. 294 (2006) 205–220. doi:10.1016/j.jsv.2005.11.014.

[77] T. A. N. Silva, N. M. M. Maia, J. I. Barbosa, A model updating technique based on FRFs for damped structures, in: Proc. ISMA/USD 2012, Katholieke Univ Leuven, 2012, pp. 2213–2226.

[78] S.-H. Jo, H. Yoon, Y. C. Shin, W. Choi, C.-S. Park, M. Kim, B. D. Youn, Designing a phononic crystal with a defect for energy localization and harvesting: Supercell size and defect location, Int. J. Mech. Sci. 179 (2020) 105670. doi:10.1016/j.ijmecsci.2020.105670.

[79] F. Akbari-Farahani, S. Ebrahimi-Nejad, From defect mode to topological metamaterials: A state-of-the-art review of phononic crystals & acoustic

metamaterials for energy harvesting, Sens. Actuators, A 365 (2024) 114871. doi:10.1016/j.sna.2023.114871.

[80] A. Barbosa, N. Kacem, N. Bouhaddi, Standing Solitons Tuned by Impurities in Damped Nonlinear Lattices under External Excitation, Phys. Rev. Lett. 133 (2024) 187201. doi:10.1103/physrevlett.133.187201.

[81] R. R. Craig, A. Kurdila, Fundamentals of structural dynamics, Wiley, 2006.

[82] F. M. Gruber, D. J. Rixen, Evaluation of Substructure Reduction Techniques with Fixed and Free Interfaces, Strojniški vestnik - Journal of Mechanical Engineering 62 (2016) 452–462. doi:10.5545/sv-jme.2016.3735.

[83] J.-M. Mencik, Improved model reduction with basis enrichment for dynamic analysis of nearly periodic structures including substructures with geometric changes, J. Comput. Appl. Math. 445 (2024) 115844. doi:10.1016/j.cam.2024.115844.

[84] Ansys®, Mechanical APDL 2024 R2, Structural Analysis Guide, 3.9. Modal Analysis Tools for Subsequent Mode-Superposition Analysis, ANSYS, Inc., 2024 [accessed 09 December 2024].

[85] Ansys®, Mechanical APDL 2024 R2, Theory Reference, 14.8. Mode-Superposition Method, ANSYS, Inc., 2024 [accessed 09 December 2024].

[86] K. Mizukami, K. Funaba, K. Ogi, Design and three-dimensional printing of carbon-fiber-composite elastic metamaterials with inertial amplification mechanisms, J. Sound Vib. 513 (2021) 116412. doi:10.1016/j.jsv.2021.116412.

[87] V. Santos, T. Paula Sales, Numerical investigation of a zig-zag beam-type quasi-periodic structure with multiple defects, in: Proc. XIX Int. Symp. Dynamic Probl. Mech., DIN2023, ABCM, 2023, pp. 1–10. doi:10.26678/abcm.diname2023.din2023-0170.

[88] S.-K. Hong, B. I. Epureanu, M. P. Castanier, D. J. Gorsich, Parametric reduced-order models for predicting the vibration response of complex

structures with component damage and uncertainties, J. Sound Vib. 330 (2011) 1091–1110. doi:10.1016/j.jsv.2010.09.022.

[89] S.-K. Hong, B. I. Epureanu, M. P. Castanier, Next-generation parametric reduced-order models, Mech. Syst. Signal Pr. 37 (2013) 403–421. doi:10.1016/j.ymssp.2012.12.012.

[90] M. I. Friswell, J. E. Mottershead, Finite Element Model Updating in Structural Dynamics, Springer Dordrecht, 1995. doi:10.1007/978-94-015-8508-8.